

1 **Thrusts control the thermal maturity of accreted sediments.**

2 Utsav Mannu^{1,5,*}, David Fernández-Blanco², Ayumu Miyakawa³, Taras Gerya⁴, and Masataka Kinoshita⁵

3 ¹Discipline of Earth Sciences, Indian Institute of Technology, Gandhinagar [382355](#), India;

4 ² Barcelona Center ~~of~~ Subsurface Imaging, ~~Institut~~ [Passeig Marítim de Ciències del Mar \(ICM-](#)
5 [CSIC\)](#), [Barceloneta 37-49](#), Barcelona, Spain;

6 ³~~Geological~~ [Geological](#) Survey of Japan, AIST, [Central 7, Higashi 1-1-1, Tsukuba, Ibaraki, 305-8567, Japan](#)

7 ⁴Institute of Geophysics, [Department of Earth Sciences, ETH Zurich, Sonneggstrasse, 5, 8092 Zurich, Switzerland](#)

8 ⁵Earthquake Research Institute, ~~UTokyo~~ [The University of Tokyo, 1-1-1 Yayoi Bunkyo-ku, Tokyo, 113-0032,](#)
9 [Japan](#)

10 **Correspondence to: Utsav Mannu (utsav.mannu@iitgn.ac.in)*

11

12

13

14

15

16

17

18

19

20

21

22 **Abstract.**

23 Thermal maturity assessments of hydrocarbon-generation potential and thermal history rarely consider how upper-
24 plate structures developing during subduction influence the trajectories of accreted sediments. Our
25 thermomechanical models of subduction support that thrusts evolving under variable sedimentation rates and
26 décollement strengths fundamentally influence the trajectory, temperature, and thermal maturity of accreting
27 sediments. This is notably true for the frontal thrust, which pervasively partitions sediments along a low and a high
28 maturity path. Our findings imply that interpretations of the distribution of thermal maturity cannot be detached
29 from accounts of the length and frequency of thrusts and their controlling factors. Our approach takes these factors
30 into consideration and provides a robust uncertainty estimate in maximum exposure temperatures as a function of
31 vitrinite reflectance and burial depth. As a result, our models reduce former inconsistencies between predicted and
32 factual thermal maturity distributions in accretionary wedges.

33

34

35

36

37

38

39

40

41

42

43

44
45

46 **1. Introduction**

47 Organic material transforms into coal, oil, and gas at rates primarily controlled by temperature. This transformation,
48 critical for the hydrocarbon industry, is also useful to study the tectonic and sedimentary evolution of basins and
49 orogens. The extent of this transformation in sediments, known as thermal maturity, can be measured as vitrinite
50 reflectance, i.e., the percentage of incident light reflected from the surface of vitrinite particles in those sediments.
51 Thermal maturity has been used to estimate the thermal evolution of igneous intrusions and seismic slip, the extent
52 of low-grade metamorphism, porosity, and compaction in basin sediments, and the geothermal history of accreting
53 material during subduction (e.g., Bostick and Pawlewicz, 1984; Rabinowitz et al., 2020; Fukuchi et al., 2017;
54 Kamiya et al. 2017).

55 Inferences on the geothermal history of subduction margins based on thermal maturity depend on the
56 trajectory followed by the accreting sediments (Miyakawa et al., 2019). Low-temperature, high-pressure
57 metamorphic rocks in the subduction wedge are often attributed to the pressure maxima that typically predate the
58 temperature maxima in accreted sediments undergoing diagenesis in the wedge (~~Rub, 2020~~ [van Gool and Cawood,
59 1994](#)). However, the existence of complicated patterns in sediment trajectories is supported by numerical models
60 and field observations (Giunchi & Ricard, 1999). As the orogenic wedge evolves, sediments accreting along
61 different paths reach different depths and velocities and are exposed to different regional peak temperatures.
62 Miyakawa et al. (2019) proposed to subdivide these trajectories based on their final characteristics, like thermal
63 maturity. In this manner, the spatiotemporal evolution of sediments and their thermal maturity is regulated to a first
64 order by the partition of incoming sediments along two endmember pathways; (I) a deeper path leading to elevated
65 thermal maturities and constituted by underthrust material, the *high thermal-maturity path*, and (II) a shallower

66 path that typically lies closer to the surface or gets frequently exhumed to near-surface levels, the *low thermal-*
67 *maturity path*.

68

69 Previous studies have used numerical and analogue approaches to study the trajectories of sedimentary
70 particles, and their spatial and pressure-temperature evolution, as a function of changes in erosion, sedimentation,
71 or décollement strength. The trajectory followed by underthrust sedimentary units is primarily determined by
72 orogenic wedge dynamics and its controlling forces (Plat, 1986). Although these sediments may only be exhumed
73 near the backstop of the wedge, the trajectories of other accreted sediments generally deflect toward the surface
74 under the influence of erosion (Konstantinovskaia and Malavieille, 2005). In fact, sedimentary particle trajectories
75 gradually shift from deflection toward the surface near the front of accretion to final exhumation near the wedge
76 backstop (Wenk and Huhn, 2013). Still, even under-thrust sediments, which would co-relate to high-maturity
77 paths in our study, have variable pressure-temperature paths (Ruh, ~~2020~~2020). It is important to highlight that the
78 majority of past studies have explored a snapshot of sediment trajectories, assuming that the general nature of
79 trajectories remains relatively fixed with time or is stationary in nature. However, the intrinsic connection between
80 thermal maturity and the comprehensive thermal exposure along the entire trajectory necessitates an in-depth
81 investigation into the dynamic and transitory nature of sediment trajectories.

82 Although there is general consensus on the rate and extent of sediment trajectory transition from horizontal
83 to vertical during accretion, the dynamic perturbations in sediment dynamics have yet to be adequately examined.
84 For instance, while most studies show a great degree of correlation between the initial depth of incoming sediments
85 and their final position in the wedge (e.g., Mulugeta and Koyi, 1992; Willett, 1992), a dynamic fluctuation in this
86 correlation due to thrusting can result in non-stationary exhumation paths for accreting sediments in a wedge (e.g.,

87 Konstantinovskaia and Malavieille, 2005; Miyakawa et al., 2019). Much remains to be explored regarding the
88 partition of high and low thermal maturity paths and how sediments travel inside natural wedges, given the
89 conventional assumption that accreting sediments remain at the same relative depth and translate along the adjacent
90 “layers” without vertical mixing throughout the tectonic evolution of the wedge (Hori and Sakaguchi, 2011).

91 Our assessment identifies a primary gap in existing research: the prediction and mapping of the initial
92 sediment influx to their ~~final~~ location in the orogenic wedge. More specifically, the challenge lies in determining
93 which portions of incoming sediment will predominantly constitute the core of the wedge and which will reside at
94 comparatively shallower depths. Given that the maximum exposure temperature estimation from the thermal
95 maturity is inherently reliant on the path of sediments inside the wedge, information on path diversity would
96 inherently constrain the uncertainty in maximum exposure temperature used for the identification of paleothermal
97 structures of subduction zones. Moreover, to better understand the time-depth paths of wedge sediments, their
98 dependence on the initial state of undeformed sediments, and thus their thermal maturity, the factors that control
99 the evolution of subduction-accretion systems, like sedimentation, erosion, and décollement strength, ought to be
100 considered (Mannu et al., 2016; Simpson, 2010).

101 Here, we explore in detail the impact of accretion in a subduction wedge has on the thermal maturity of its
102 sediments. We simulate subduction-accretion using 2D finite-difference thermomechanical models incorporating
103 empirical thermal conductivity values from the Nankai accretionary margin. We track the evolution of thermal
104 maturity by computing vitrinite reflectance (%R_o) on each marker and throughout the model, using three well-
105 established methods of %R_o computation, as accretion develops the wedge under different sedimentation rates and
106 décollement strengths. These factors notably alter the trajectories and thermal maturities of incoming sediments.
107 Particularly, thrusts define sharp thermal maturity boundaries leading to stark differences in the thermal maturity
108 of sediments that accrete in different thrust blocks, even when they follow similar trajectories and lay nearby.

109 **2. Geological settings and model generalization**

110 We use a generalized model for the subduction of an oceanic plate under a continental plate, with explicit
111 integration of key parameters from the Nankai subduction margin off the Kii island in southwest Japan. The Nankai
112 subduction margin is a product of the ongoing, northwest-directed subduction of the Philippine Sea Plate beneath
113 the Amurian Plate at a convergence rate of 4.1-6.5 cm/yr (Seno et al., 1993; Miyazaki and Heki, 2001; DeMets et
114 al., 2010). Past studies posit the initiation of this subduction within the Nankai region at circa 6 Ma (Kimura et al.,
115 2014). The accretionary wedge adjacent to the Nankai margin is marked by the accretion of ~~extensive~~thick sediment
116 layers (>1 km), predominantly formed by overlying younger trench sediments atop Shikoku Basin sediments. Mean
117 sedimentation rates of ~0.4 mm/yr for this area are calculated from sediment data onland and may largely reach the
118 trench through submarine channels (Korup et al., 2014).

119 Another reason to select the Nankai subduction margin is that it is a particularly well-studied accretionary margin
120 regarding its paleo-thermal history and thermal maturity distribution. For example, Underwood et al. (1993) and
121 Sakaguchi (1999) used thermal maturity estimates from Shimanto accretionary wedge in the Nankai subduction
122 margin to suggest that ridge subduction can explain the resulting paleo-heat flow. Following this, Ohmori (1997~~7~~)
123 published a distribution of thermal maturity and maximum exposure temperature for the Shimanto accretionary
124 wedge identifying out-of-sequence ~~activity~~thrusting in the region. The accretionary wedge adjacent to the Kumano
125 forearc basin in the Nankai subduction margin has also been the subject of the NanTroSEIZE (Nankai Trough
126 Seismogenic Zone) project, which drilled C0002 borehole during the 2012 Integrated Ocean Discovery Program
127 Expedition 338. C0002 borehole is located approximately km southwest of Japan's Kii Peninsula in the Kumano
128 Basin, within the Nankai accretionary margin, and extends 3,348 meters below the seafloor. Having data on both
129 thermal maturity and thermal conductivity from the same borehole in subduction wedges is quite uncommon. To
130 our knowledge, the C0002 borehole, located next to the Kumano forearc basin, is the only place where such data

131 can be found in an accretionary wedge. Because of this unique characteristic, the C0002 borehole serves as an
132 excellent dataset for validation purposes. We modify the thermal conductivity computation for sediments and
133 décollement (see Table 1) to match the empirical relationship between depth and thermal conductivity, as measured
134 on core samples in the borehole C0002 (Sugihara et al., 2014).

135 While these adjustments render our models somewhat specific to the Nankai accretionary wedge, we propose that
136 the thermal conductivity values and trend are representative of patterns typically observed in forearc basins and
137 accretionary wedges across the globe, making it broadly applicable to general subduction margins. For instance, in
138 our simulations, the sediment thermal conductivity within our wedge steadily increases with depth from 0.96-4.0
139 $\text{Wm}^{-1}\text{K}^{-1}$, which is within the range of thermal conductivity estimates for comparable depth in other subduction
140 zones, such as the Hikurangi subduction margin, Japan Trench, and Taiwan subduction zone (Fig. S1, Henrys et
141 al. 2003, Lin et al. 2014, Chi and Reed, 2008). As a result, we compare our simulation results not only to thermal
142 maturity values in the Nankai accretionary margin but also to those of the Miura-Boso plate subduction margin in
143 central Japan and the fold and thrust belts of the Western Foothills complex in western Taiwan.

144 **3. Methods**

145 We employ I2VIS, a conservative finite-difference 2-D thermomechanical subduction-accretion model with visco-
146 plastic/brittle rheology (Gerya and Yuen, 2003a, 2003b). The code solves the governing equations for the
147 conservation of mass, momentum, and heat as well as the advection equation with a non-diffusive marker-in-cell
148 scheme constrained by thermal conductivity values inferred from Nankai accretionary wedge. Our numerical
149 approach has several advantages over earlier attempts to simulate thermal maturity in an accretionary wedge, such
150 as a more realistic geothermal profile, variable particle paths, and thermal evolution. In the following sections, we
151 provide information regarding the governing equations, the modified thermal conductivity formulations based on

152 the C0002 borehole, boundary conditions, the rheological model, model setup, surface processes, and the
153 computation of thermal maturity.

154 3.1 Governing equations

155 The mass conservation is described by the continuity equation with the Boussinesq approximation of
156 incompressibility.

$$157 \quad \frac{\partial v_x}{\partial x} + \frac{\partial v_y}{\partial y} = 0 \quad (\text{eq. 1})$$

158 ~~and the~~ Where v_x and v_y are horizontal and vertical components of velocity.

159 The equation for conservation of momentum with an incompressibility assumption is expressed in the 2D-
160 ~~stokes~~Stokes equation, for the x -axis and y -axis, respectively,

$$161 \quad \frac{\partial \sigma_{xx}}{\partial x} + \frac{\partial \sigma_{xy}}{\partial y} = \frac{\partial P}{\partial x} \quad (\text{eq. 2})$$

162 where σ_{xx} , σ_{xy} , σ_{yy} are components of the deviatoric stress tensor; x and y denote the horizontal and vertical
163 coordinates and P is pressure.

$$164 \quad \frac{\partial \sigma_{yy}}{\partial y} + \frac{\partial \sigma_{xy}}{\partial x} = \frac{\partial P}{\partial y} - g\rho(T, P, C, M) \quad (\text{eq. 3})$$

165 ~~Where density $\rho(T, P, C, M)$ depends on temperature (T), pressure (P), composition (C), and mineralogy (M).~~

166 where ρ is rock density and depends on rock type(C), temperature(T), and pressure as $\rho(T, P) = \rho_0(1 -$
167 $\xi(T - T_0))(1 + \zeta(P - P_0))$ where ξ is the coefficient of thermal expansion taken to be $3 \times 10^{-5} \text{ K}^{-1}$ for all rock

Formatted: Font color: Auto

168 markers and 0 for air/water, ζ is the coefficient of compressibility is taken to be $1 \times 10^{-5} \text{ MPa}^{-1}$ for all rock markers
 169 and 0 for air/water, ρ_0 is the reference density at reference temperature ($T_0 = 298.15 \text{ K}$) and reference pressure
 170 ($P_0 = 10^5 \text{ K}$).

171 The thermal equation used in the model is as follows:

172
$$\rho C_p \frac{DT}{Dt} = \frac{\partial q_x}{\partial x} + \frac{\partial q_y}{\partial y} + H_r + H_a + H_s + H_t \quad \text{(eq. 4)} \quad \text{(eq. 4)}$$

173 where,

174
$$q_x = -k(T, C, Z)(T, C, y) \frac{\partial T}{\partial x}, \quad q_y = -k(T, C, Z)(T, C, y) \frac{\partial T}{\partial y} \quad \text{(eq. 5)}$$

175
$$H_a = T\alpha T \xi \frac{DP}{Dt}, \quad H_s = \sigma_{xx} \dot{\epsilon}_{xx} + \sigma_{yy} \dot{\epsilon}_{yy} + \sigma_{zz} \dot{\epsilon}_{zz} \quad \text{(eq. 6)} \quad \dot{\epsilon}_{xx} + \sigma_{yy} \dot{\epsilon}_{yy} + \sigma_{xy} \dot{\epsilon}_{xy} + \sigma_{yx} \dot{\epsilon}_{yx}, \quad H_r =$$

 176
$$\text{const} \quad \text{(eq. 6)}$$

177 Where $\frac{D}{Dt}$ is the Lagrangian time derivative, and x and y denote the horizontal and vertical coordinates,
 178 respectively; $\sigma_{xx}, \sigma_{yy}, \sigma_{zz}$ are components of the deviatoric stress tensor; $\dot{\epsilon}_{xx}, \dot{\epsilon}_{yy}, \dot{\epsilon}_{zz}$ are
 179 components of the strain rate tensor; P is pressure; T is temperature; q_x, q_y are the components of heat flux in the
 180 horizontal and vertical direction; ρ is density; g is the vertical gravitational acceleration; C_p is the isobaric heat
 181 capacity; H_r, H_a, H_s, H_t denote the radioactive, adiabatic, and shear and latent heat production, respectively.
 182 $k(T, C, Z)(T, C, y)$ is the thermal conductivity, a function of composition, depth, and temperature (Table 1). The
 183 radioactive heat production H_r is constant for a rock type as mentioned in Table 1.

184 In order to accurately assess thermal maturity, it is crucial to consider the temperature distribution, which
185 necessitates a realistic thermal conductivity profile when modeling thermal maturity. Many geodynamic models
186 assume that thermal conductivity decreases as temperature increases, following a defined relationship (e.g., Clauser
187 and Huenges, 1995). These models typically predict a decrease in thermal conductivity with depth within
188 accretionary wedges, as geothermal profiles tend to increase in temperature with depth. However, empirical data
189 reveal a different trend: thermal conductivity increases with depth, primarily due to sediment porosity influencing
190 shallow thermal conductivity (Henry et al. 2003, Lin et al. 2014). Additionally, the thermal conductivity values
191 calculated using the Clauser and Huenges model (1995) are significantly higher than those observed at shallow
192 depths (< 3 km). To address these disparities, we incorporate the observed empirical relationship between depth
193 and thermal conductivity from the IODP Site C0002 borehole in the Nankai accretionary wedge into our
194 simulations. By adjusting the thermal conductivity formulation for sediments based on temperature and depth, we
195 aim to replicate the empirical relationship observed in the core samples taken from the borehole at IODP Site C0002
196 (Sugihara et al., 2014) and account for the decrease in thermal conductivity near the surface caused by increased
197 porosity. We modify the thermal conductivity formulation for sediments as a function of temperature and depth as
198 follows.

199

$$k_{sed} = k_0 + \frac{807}{T + 77} \left(1 - \exp\left(\frac{-Z^2}{1.3e^7}\right) \right) \quad (eq. 6)$$

200 $k_0 = 0.96$ and 1.5 for the wedge sediment and décollement respectively. The larger thermal conductivity of the
201 décollement emulates higher heat transfer in shear zones due to fluid advection (Fig. S1).

202 **3.2 Rheological model**

203 The expression for effective creep viscosities (η_{eff}) is computed as follows.

$$\eta_{dist} = 0.5(\varepsilon_{II})^{\frac{1}{n}-1} A_D^{\frac{1}{n}} h^m \exp\left(-\frac{E_a + V_a P}{nRT}\right) \exp\left(-\frac{E_a + V_a P}{nRT}\right) \quad (eq. 7)$$

$$\eta_{diff} = 0.5 \frac{A_D}{S^{n-1}} \exp\left(-\frac{E_a + V_a P}{RT}\right) \quad (eq. 8)$$

$$\eta_{eff} = \left(\frac{1}{\eta_{dist}} + \frac{1}{\eta_{diff}}\right)^{-1} \quad (eq. 9)$$

where P is pressure (Pa), T is the temperature (K), R is the gas constant (8.314 J/K/mol), h is grain size (m) and, A_D, n, m, E_a and V_a are experimentally determined rheological parameters: A_D is the material constant ($\text{Pa}^{-n} \text{s}^{-1} \text{m}^{-m}$), n is the stress exponent, m is the grain size exponent, E_a is activation energy (J/mol), V_a is activation volume (J/Pa), and S is a stress factor for diffusion creep. ~~As dislocation creep does not depend on grain size, therefore, we assume $h^m = 1 - c_{II}$ is the second invariant of strain tensor computed as assumed to be $3 \times 10^4 \text{ Pa}$.~~

$$\varepsilon_{II} = \sqrt{\frac{\dot{\varepsilon}_{ij} \cdot \dot{\varepsilon}_{ij}}{2}} \quad (eq. 10)$$

The model uses visco-plastic rheology to account for both brittle rheology of the shallower and colder rigid lithosphere and deeper, hotter ductile lithosphere and asthenosphere. Using the plastic yield threshold as per the Drucker-Prager criterion we limit effective viscosity as

$$\eta_{eff} \leq \frac{P \cdot \sin \varphi \cdot (1 - \lambda) + C \cdot \cos \varphi}{2\varepsilon_{II}} \quad (eq. 11)$$

~~Where C is cohesion and φ is an effective internal angle of friction or $\mu = \tan \varphi$ where is the coefficient of internal friction and λ the fluid pressure ratio- assumed to be 0 in all the simulations.~~

219 **3.3 Boundary conditions**

220 A free-slip boundary condition is implemented on all boundaries, except on the lower boundary, which is
221 ~~passable~~impermeable in the vertical direction. ~~Where~~On the lower boundary we implement an external free slip
222 condition similar to where a free slip condition is satisfied at an external boundary such that

223
$$\frac{\partial V_x}{\partial x} = 0, \text{ and } \frac{\partial V_y}{\partial y} = \frac{V_y}{\Delta Y_{external}} \quad (\text{eq. 10})$$

224 Where, V_x and V_y , are the velocities in the horizontal and vertical directions at the boundary, $\Delta Y_{external}$ is the depth
225 that lies outside the modeling domain, and where free slip condition is maintained. Similarly, we set thermally
226 insulating boundary conditions on all sides except the lower one where the external thermal boundary condition is
227 implemented.

228 **3.4. Surface processes**

229 The rock-water/air boundary is simulated by an adaptive irregular grid that is advected horizontally and vertically
230 and is coupled to the thermomechanical grid which controls the tectonic ~~change~~deformation of the surface. Apart
231 from the tectonic changes, surface processes prescribed in the model can also change the topography. The surface
232 process in the model is controlled by the conversion of rock markers to air/water and vice versa. All sedimentation
233 in the model happens as a focused deposition of sediments from sea to land in morphological depressions (e.g.,
234 trench) is modelled as follows (Fig. S2)

235
$$V_{new} y_{new} = V_{old} y_{old} + K \cdot V_{fill} \cdot y_{fill} \quad (\text{eq. 11})$$

236 ~~Where~~where $K = \min \left(\frac{V_{budget}}{V_{basin}}, 1 \right)$

237 The shape of the basin and the resolution of the surface grid can lead to overfilling or underfilling when using the
238 equation mentioned above to fill the basin. To address this issue, we calculate the volume of deposited sediments
239 and adjust for any deficit or overfill in the subsequent step. This ensures that, over time, the total amount of
240 sedimentation remains consistent with the prescribed value. However, it is challenging to ensure that all sediments
241 added in a particular step are accommodated within the basins, especially in models with high sedimentation rates
242 where significant runoff occurs. Therefore, the sedimentation rates mentioned in this study are computed as
243 effective sedimentation rates after the model runs, rather than being predetermined. We perform multiple models
244 runs (approximately 100) with sedimentation rates uniformly distributed in the range of 0.1-0.9 mm/yr. From these
245 runs, we select models that exhibit appropriate sedimentation rates. This selection process ensures that the average
246 sedimentation rates across all our models (ranging from 0.1-0.9 mm/yr) fall within the observed sedimentation rates
247 in our chosen natural equivalent, the Nankai accretionary wedge in the southwestern subduction margin of Japan
248 (Korup et al., 2014). For more specific information about the model run and prescribed sedimentary conditions,
249 please refer to Table 2

250 ***3.5 Thermal maturity calculation***

251 The model computes the %R_o of each marker to estimate the thermal maturity of sediments during the model run
252 using three widely used methods of thermal maturity modelling Easy%R_o (Burnham and Sweeney, 1989, Sweeney
253 and Burnham 1990), Simple%R_o (Suzuki et al., 1993) and Basin%R_o (Nielsen et al., 2017). All the models
254 presented here employ a simplified parallel Arrhenius reaction model, which accommodates an array of activation
255 energies for every component of the kerogen, allowing it to estimate thermal maturity under varying temporal and
256 thermal scales. The Easy%R_o model by Sweeney and Burnham (1990) can be described using the following
257 equations:

258

$$x_i(t) = x_{oi} \exp\left(-\int A \exp\left(-\frac{E_{ai}}{RT(t)}\right) dt\right) \quad (eq. 12)$$

259

$$X(t) = \sum_{i=1}^N x_i(t) \quad eq. 13$$

260

$$F(t) = X(t = 0) - X(t) \quad (eq. 14)$$

261

$$\%R_o = \%R_{o0} \exp(3.7F) \quad (eq. 15)$$

262

263

264

265

266

267

268

269

Where, x_{oi} are weights of reactions for i^{th} component of the kerogen also described as the stoichiometric coefficient, A is the pre-exponential factor, E_{ai} is the activation energy of the i^{th} component of the kerogen, R is the gas constant, $T(t)$ is the temperature history, F is the amount of fixed carbon as a percentage and $\%R_{o0}$ is the vitrinite reflectance of the immature unaltered sediment. Sweeney and Burnham (1990) provided a set of 20 activation energies (E_{ai}) and the stoichiometric coefficient (x_{oi}) listed in Table 3. All thermal models used in this study use the same method of vitrinite reflectance computation albeit with different sets of activation energies, stoichiometric coefficient, pre-exponential factor and $\%R_{o0}$. Table 3 provides a comprehensive list of all these parameters.

270

271

272

273

274

275

276

All these approaches for computing $\%R_o$ yield similar trends albeit with different absolute values. In the interest of clarity, we have mostly illustrated Easy $\%R_o$, which is the most extensively used method for Vitrinite Reflectance computation and hereafter we refer Easy $\%R_o$ as $\%R_o$, unless explicitly stated. $\%R_o$ is set to $\%R_{o0}$ in sediment markers at the start of the model till 2.5 Myr, while $\%R_o$ in markers for other rocks, air, and water is undefined at all times. After 2.5 Myr, the model computes $\%R_o$ on each marker as a function of temperature (T), time (t), and amount of fixed carbon as a percentage (F). The initial $\%R_o$ of newly deposited sediments is computed using an assumed water-sediment interaction temperature assumed to be the same as the thermocline. The thermocline used

277 in the model has been estimated using the data obtained and made freely available by International Argo Program
278 and the national programs that contribute to it for the region near Nankai (Fig. S3; <https://argo.ucsd.edu>,
279 <https://www.ocean-ops.org>).

280 **3.5 Model ~~Set-up~~ Setup**

281 The modelling domain is 3500 km wide and 350 km deep and is ~~discretized~~ divided into 3484×401 nodes populated
282 with ~125 million markers (Fig. 1). The high resolution of 220 m (horizontal) \times 130 m (vertical) that we assign at
283 the site of accretionary wedge evolution, decreases steadily toward the edges of the modelling domain to a
284 minimum resolution of 3000 m \times 3200 m. The simulation consists of an oceanic plate converging with a velocity
285 of ~5 cm/yr and subducting beneath a continental plate (Fig. 1). The convergence is prescribed internally using
286 highly viscous nodes inside the oceanic and continental plates near the boundary of the models. The oceanic plate
287 consists of a 1-km-thick upper oceanic crust and a 7-km-thick lower crust- (Akuhara, 2018). The thickness of the
288 oceanic lithosphere depends on its age which is set to 20 Myr at the start of the simulation (Turcotte and Schubert,
289 2002). The initial age of the oceanic lithosphere corresponds to the age of the subducting lithosphere in the Nankai
290 subduction margin (Zhao et al. 2021). Displacement along the megathrust, at the contact between subducting
291 oceanic plate and the overriding continental plate, occurs in a relatively weak basal layer in accretionary wedges
292 across the globe (Byrne and Fisher, 1990). We simulate this with a predefined configuration at the interplate, with
293 a 350-meter-thick weak décollement below a sediment layer that is a km thick. The wedge forms above this
294 interphase by the accretion of sediments against the continental plate. The continental plate consists of an upper
295 and lower continental crust with thicknesses of ~20 km and ~15 km, respectively- (Akuhara, 2018), and is underlain
296 by a mantle lithosphere of ~25 km. We use a thin (10 km) "sticky air" layer to overlay the top face of the rock strata
297 inside the model which is a fluid with a low viscosity of 5×10^{17} Pa-s, and a low density, similar to air (white in Fig.
298 1) or water (light blue in Fig. 1) (Cramer et al., 2012). The transition between the lithosphere and asthenosphere

299 is prescribed to occur at 1300°C. A weak layer is emplaced at the junction of both plates, which fails mechanically
300 and leads to subduction initiation. All sediments (light and dark brown in Fig. 1) are rheologically identical, but
301 colours are alternated in time to allow tracking the development of different geological structures. Readers are
302 referred to Table 1 for the rheological and thermal properties of all the materials used. Note that in our models, we
303 refer to the measure all distances from the point where the continental and oceanic plates initially and is situated
304 1850 km from the right boundary of the modelling area. The terms "landward" and "seaward" indicate the relative
305 direction towards the continental plate or the oceanic plate, respectively. The "Backstop" refers to the edge of the
306 continental plate that buttresses the wedge and acts akin to an indenter for the accretionary wedge. The "forearc
307 high" represents the highest point in the forearc zone, which includes both the accretionary wedge and the forearc
308 basin.

309

310 *3.6 Experimental Strategy*

311 Here, we present a total of 10 ~~model~~simulations that vary in their effective basal friction or their effective
312 sedimentation rate to discern patterns of thermal maturity evolution in wedge sediments. Models $M_0^{4.5} - M_0^{14.5}$
313 have no sedimentation and effective internal angle values for the décollement of $\varphi_b = 4.5^\circ, 7^\circ, 9.5^\circ, 12^\circ$ and 14.5°
314 respectively. The chosen range of effective décollement strength is well within the range of values postulated by
315 several studies for the Nankai accretionary wedge (Tesei et al., 2015). The rest of the models ($M_{0.1}^{9.5} - M_{0.9}^{9.5}$) and
316 have a medium-strength décollement and variable effective sedimentation rate ranging from 0.1 to 0.9 mm/yr. In
317 all the models presented in this study, sedimentation is limited to the trench, extending from the sea to the land.
318 Restricting sedimentation to the trench allows us to observe and ~~analyse~~analyze the length and frequency of thrust
319 sheets, enabling comprehensive investigation of their role in determining sediment trajectories. With these models,
320 we evaluate the particle trajectory and %R_o of accreting sediments as a function of décollement strength and
321 sedimentation rate. To restrict the number of parameters influencing our observations, models have no erosion.

322 Moreover, all models lack surface processes during the first ~2.5 Myr and have sedimentation thereafter. Strain-
323 softening has been modeled as a linear decrease of angle of friction (φ) and cohesion between cumulative strain of
324 0.5 and 1.5. Sediments used in the model have an angle of friction (φ) of 30° before a cumulative strain of 0.5 and
325 a strain-softened value of 20° after a threshold of 0.5-1.5 cumulative strain. The coefficient of friction ($\tan \varphi$)
326 increases linearly between Strain softening has been used in wedges to mimic the strain thresholds weakening of
327 faults and shear zones due to lubrication with values threshold taken from previous numerical studies (Hickman et
328 al., 1995, Ruh et. al. 2014).

329 4. Results

330 In our models, subduction begins at 0.1 Myr by failure of the weak material between continental and oceanic plate
331 (Fig. 2, Fig. S4-S13, also [see supporting information movies](#)). Continued and sustained accretion of sediments
332 against the deforming continental crust forms the accretionary wedge from the interplate contact landwards. After
333 ~5 Myr, all models develop a distinct wedge in agreement with the critical wedge theory (Davis et al., 1983).
334 Surface slopes, measured by fitting a line in the surface of the wedge for every timestep between 2.5-7.5 Myr and
335 reported as mean \pm standard deviation, increase systematically, as effective basal friction increases from $\sim 4.5^\circ$ to
336 $\sim 14.5^\circ$ (Fig. 1, Fig S4-S13, Table 2, $M_0^{4.5} - M_0^{14.5}$). Whereas models with a relatively weaker décollement, as
337 ($M_0^{4.5}, \varphi_b = 4.5^\circ$), have surface slopes of $0.95^\circ \pm 0.3^\circ$, models with very strong décollement, as ($M_0^{14.5}, \varphi_b = 14.5^\circ$),
338 have slopes as steep as $5.9 \pm 1^\circ$ (Table 2). Our estimations of surface slopes consistently exhibit an excess of
339 approximately 1.5° compared to the surface slopes predicted by the critical wedge theory (Table 2). This is probably
340 due to the penetration of weaker décollement material into high shear zones, resulting in faults that are weaker than
341 the strain-softened wedge material.

343 Models without trench sedimentation grow solely by accretion of incoming seafloor sediments, with frequent
344 nucleation of frontal thrusts. Models with weaker décollements develop thrust sheets that are lengthier but remain
345 active for shorter periods. This is clear when comparing, for models with increasingly strong décollement
346 ($M_0^{4.5}, M_0^7, M_0^{9.5}, M_0^5, M_0^{14.5}$), the average distance between first and second frontal thrusts are 15.5 ± 7.0 km, 12.1
347 ± 3.6 km, 8.8 ± 3.3 km, 8.7 ± 2.1 km and 8.0 ± 1.8 km, respectively. Increasing sedimentation rate also leads to an
348 increase in thrust sheet length from 7.3 ± 1.1 km for model $M_{0.1}^{9.5}$ to 13.8 ± 7.8 km in model $M_{0.9}^{9.5}$.

349

350 In models with similar basal friction, models with higher sedimentation rates have lengthier thrust sheets that
351 remain active for longer periods (Table 2). Steeper surface slopes with increased décollement strengths and change
352 in thrust sheet length with sedimentation and décollement strength are well-known effects that have been
353 confirmed by previous numerical ([Ruh et al., 2012](#)) and ~~analytical~~analogue (Malavieille and Trullenque, 2009;
354 Storti and McClay, 1995) models. All the reported values are mean \pm Standard Deviation values recorded between
355 2.5-7.5 Myr in individual models. All models exhibit a temperature gradient that corresponds well with the
356 temperature profile observed in the boreholes at IODP Site C0002 in the Kumano forearc basin, on top of the
357 Nankai accretionary wedge (Fig. S14).

358

359 ***4.1 Thermal maturity of the wedge***

360 Sediments are more thermally mature in wedges that have a higher sedimentation rate or décollement strength. For
361 example, the mean %R_o of simulations for wedges with the highest sedimentation is 12% higher (0.75) than in
362 those without sedimentation ($M_0^{4.5}$, Table 2, Fig. 3). Similarly, simulations of wedges with the strongest
363 décollement have the highest mean %R_o (0.94) of all the simulations presented in this study.

364 Thermal maturity values increase with depth and landward distance from the trench to the forearc high
365 irrespective of the décollement strength, sedimentation rates and method of thermal maturity computation (Fig. 3-
366 4). The absolute value of $\%R_o$ and the rate at which thermal maturity values increase landward from the trench are
367 larger for wedges with high décollement strength (Fig. 4A). For wedges characterized by the same décollement
368 strength but higher trench sedimentation, we observe that the rate of thermal maturity increases in a landward
369 direction from the trench and remains consistent across these wedges (Fig. 4B). Comparing the values of $\%R_o$
370 along a horizontal marker at the depth of trench in several models emphasizes this result; the model with the highest
371 décollement strength reaches a maximum $\%R_o$ of 1.25 and has the highest rate of landward increase in thermal
372 maturity (Fig. 4A). However, all models with similar décollement strength but different sedimentation do not
373 visibly vary in their rate or magnitude of landward increase in thermal maturity. All models show a decrease in
374 thermal maturity landward of the forearc high, commonly of 0.2 $\%R_o$. Other interesting observations that we
375 explore below are the increased thermal maturity occurring in the vicinity of thrusts and the reversal in sediment
376 maturity around out-of-sequence thrust active over longer times visible across several models (e.g. Fig. 3).

377 The magnitude of $\%R_o$ varies consistently among Easy $\%R_o$, Simple $\%R_o$ and Basin $\%R_o$. On average
378 Easy $\%R_o$ have the smallest values, followed very closely by Basin $\%R_o$ (with an average difference of only 0.02).
379 However, Simple $\%R_o$ had the highest average value of thermal maturity, being 0.16 and 0.13 higher than Easy $\%R_o$
380 and Basin $\%R_o$ (Fig. 3).

381 ***4.2 Sediment trajectory inside the wedge***

382 In wedges with a higher décollement strength or sedimentation rate, sediments tend to follow high-maturity paths
383 in larger proportions. We demonstrate this effect by creating a map of the thermal maturity of sediments at 7.5 Myr
384 of the model run, mapped to their spatial position at 2.5 Myr of the model run to analyse the spatial correlation

385 between sediment position (depth and distance) from the trench and thermal maturity (Fig. 5). We also show the
386 mean thermal maturity attained by sediments at a given horizontal distance from the trench during this period by a
387 dashed black line in Fig. 5. The scatter plot shows sharp changes in eventual thermal maturity with horizontal
388 distance from the trench that relate to changes in sediment trajectory. The mean thermal maturity is also variable
389 along the horizontal length of the wedge and has a periodicity (Λ) increasing in distance with higher sedimentation
390 rate but relatively constant with changing basal friction (Fig. 5). The periodicity of mean $\%R_o$ was computed by
391 finding the average wavelength of the auto-correlated mean $\%R_o$. Whereas the mean thermal maturity has a short
392 periodicity of ~ 7.2 km for the model $M_0^{9.5}$ with no sedimentation rates, the model $M_{0.9}^{9.5}$ shows the longest periodicity
393 of 21 km. However, for all models with no sedimentation ($M_0^{4.5} - M_0^{14.5}$), the periodicity remains relatively
394 consistent between the range of 7-8 km.

395 Fig. 3 also represents the distribution of trajectories that exist in an accretionary wedge and how these
396 trajectories get impacted under trench sedimentation (a subset of these trajectories can be viewed in the
397 supplementary Fig. S15). Whereas in wedges with weak décollements ($M_0^{4.5}$), none of the shallowest half of
398 incoming sediments reach $\%R_o > 1$ in 5 Myr, 2% of sediments reach this value in wedges with strong décollement
399 ($M_0^{14.5}$). The effects of décollement strength in the thermal maturity of sediments can be quantified as well at deeper
400 levels, with one-eighth vs more than half of the sediments surpassing values of $\%R_o = 1$ for the deepest half of
401 incoming sediments (12% and 54% respectively) in weak vs strong-decollement wedges ($M_0^{4.5}$ vs $M_0^{14.5}$),
402 respectively. In wedges for the model without sedimentation ($M_0^{9.5}$), the top half of the incoming sediments
403 fail to achieve $\%R_o > 1$, as opposed to $\sim 15\%$ of them reaching $\%R_o > 1$ in the models with a sedimentation rate
404 of 0.9 mm/yr ($M_{0.9}^{9.5}$). In sum, the proportion of sediments in the top half and bottom half of the wedge that reach
405 high maturity steadily increases with both sedimentation rate and décollement strength (Table 2).

406 **4.3 Patterns of trajectory and thermal maturity in incoming sediments**

407 The diversity in the trajectory of sediments in the wedge leads to a plethora of pathways in which the sediments
408 can become thermally mature and thus introduces epistemic uncertainty in the estimation of maximum exposure
409 temperature. Fig. 6, captures this uncertainty where we plot the maximum exposure temperature as a function of
410 %R_o for all the models simulated in this study. The colours in for individual markers represent the depth of the
411 markers normalized by the thickness of the wedge represented as Y_n (See Fig S16 for mode details). We find that
412 almost all the models show a remarkable similarity in their relationship between maximum exposure temperature
413 and %R_o (for individual models please see Fig. S16) and differ mostly in their proportion of sediments with extreme
414 values of %R_o. We observe that the typical uncertainty in maximum exposure temperature increases with an
415 increase in values of %R_o with ~ 15°C interval at around %R_o=0.2 compared to ~33°C interval at %R_o= 3 (both for
416 95% confidence interval, Fig. 6b). Moreover, we observe that incorporating information about the normalized depth
417 of sediments (Y_n) significantly aids in constraining the maximum exposure temperature. For instance, although the
418 overall uncertainty at %R_o=1, is ~23°C, for sediments with a Y_n of 0.2-0.4, the uncertainty greatly reduces to only
419 ~10.5°C. Thus, the range of thermal maturity values for sediments clearly has a large correlation with their
420 trajectories.

421 **4.4 Comparison of Easy%R_o, Simple%R_o and Basin%R_o**

422 The usage of Easy%R_o, Simple%R_o, and Basin%R_o in our models provides us with a distinct perspective on the
423 comparative (dis)advantages of each method in estimating thermal maturity values. The non-uniqueness of
424 maximum exposure temperatures for the same values of %R_o arises from the variation in sediment trajectory and
425 thermal exposure. This diversity among sediment markers results in multiple markers attaining the same level of
426 thermal maturity. We refer to the range of maximum exposure temperatures corresponding to similar %R_o values

427 as the uncertainty in maximum exposure temperatures. Uncertainty for all three models increases with increasing
428 %R_o from ~20–25°C at ~0.3 to ~35°C at %R_o=3.5 (Fig. 6b). Easy%R_o, probably the best-recognised method of
429 thermal maturity computation, yields the best constraint on uncertainty for very small changes nearing <1 values.
430 For the values of %R_o between 1 and 3, all models yield very similar uncertainty, with Simple%R_o yielding the
431 most constrained exposure temperatures (Fig. 6b). However, beyond %R_o = 3, Simple%R_o becomes unreliable, with
432 uncertainty in exposure temperatures as high as 55°C at %R_o = 4. Easy%R_o yields an uncertainty range of ~37°C
433 till %R_o = 4.4, and starts to be unreliable above this value. Basin%R_o remains consistent until a very high value of
434 %R_o ~ 6, and thus provides the best constraint on the widest range of values of thermal maturity (Fig. 6b).

435 **5. Discussion**

436 The thermomechanical models presented in this study provide (a) an explanation for the trend in thermal maturity
437 observed in accretionary wedges, (b) a new venue to explore the uncertainty in the estimation of maximum exposure
438 temperature using vitrinite reflectance, and (c) an estimate of the minimum lateral distance between the trench and
439 the location of a paleo-thermal anomaly on the subduction plate for it to be identified after accretion.

440 441 **5.1 Thermal maturity distribution and importance of thrusting in wedges**

442 Collectively, our results support a general increase of thermal maturity with depth and landward in accretionary
443 wedges. The thermal maturity increase with depth is primarily the result of progressively larger exposures to higher
444 temperatures as depth of burial increases. On the contrary, the landward increase in thermal maturity is caused by
445 the long-term deformation of sediments accumulated at older times and the exhumation of sediments that were
446 underthrust as they meet the backstop. Our models demonstrate that the rate of landward thermal maturity
447 increase is faster for thicker wedges, both for the case of sediment near the surface and deep inside the wedge (Fig.
448 4). This can be attributed to a larger proportion of sediments being exposed to higher temperatures over an extended

449 duration within thicker wedges, but validating this result with natural observations remains challenging, given to
450 the very limited availability of thermal maturity data across natural wedges. Accretionary wedges in our models
451 can be simplified as a system where the subducting oceanic plate acts as the primary heat source, while the seafloor
452 acts as a heat sink. The heat generated through other sources such as shear heating, radioactivity, and advection is
453 relatively insignificant compared to the heat originating from the younger oceanic plate. In our simulations, we
454 consider a relatively younger and hotter oceanic plate of approximately 20 Myr, which is consistent with the
455 accretionary wedge in the Nankai region adjacent to the Kumano forearc basin (Zhao et al., 2021). Given that the
456 convergence rate remains constant across all models, the heat received from the oceanic plate should remain
457 relatively similar. However, as the wedge thickness increases, the temperature gradient between the boundaries of
458 the wedge must become gentler, resulting in a larger portion of the wedge experiencing elevated temperatures.
459 Moreover, frequent advection from the subduction channel also results in elevated temperatures in the core of the
460 wedge. Finally, models with thicker wedges typically exhibit higher décollement strength, leading to increased
461 shear heating at the base of the wedge. Observational studies conducted by Yamano et al. (1992) on the thermal
462 structure of the Nankai accretionary prism have further highlighted that the landward increase in prism thickness
463 is the most significant factor contributing to temperature variations within the wedge. Consequently, the sustained
464 higher temperatures within thicker wedges over time would lead to a higher rate of landward thermal maturity.

465 Our models show two cases where the above-mentioned trend in thermal maturity is relevantly altered, which we
466 nominate "on-fault increase" and "fault-block inversion". For instance, Fig. 3 shows a steep rise in the thermal
467 maturity of sediments at fault sites. Thermal maturity inversions by thrusting, which are commonplace in
468 accretionary contexts, are the primary cause of thermal maturity differentiation among wedges with similar paleo-
469 thermal structures. During fault-block inversions, the positive gradient of thermal maturity with depth is inverted
470 as relatively mature sediments are thrust over less mature sediments (Underwood et al., 1992). The strong

471 differentiation in the trajectory of sediments led by thrusting has a larger influence over thermal maturity than their
472 burial depth or their in-wedge location. This novel inference has probably remained concealed thus far due to the
473 large number of parameters that condition thrust development, frequency, length, and thermal state and the lack of
474 high-resolution thermal maturity data.

475 The thermal maturity that incoming sediments reach also varies periodically as a function of thrust frequency. By
476 examining the lateral and vertical position of incoming sediments and their eventual thermal maturity, we can
477 deduce that the overall movement of sediments in the wedge is predominantly layered but not stationary over time.
478 Changes in the depth of the thermal maturity boundary are less frequent and have larger amplitudes with increased
479 décollement strength, and especially, increased sedimentation rates (Fig. 5). The periodicity in the thermal maturity
480 boundary marks the periodic oscillation of the predominant trajectory followed by incoming sediments, i.e. between
481 accretion (low thermal maturity path) and under-thrusting (high-thermal maturity path). As a result, it should also
482 strongly correlate with the periodicity observed in the evolution of forearc topography (Menant et al., 2020) and
483 the frequency of thrust formation in our models. This is expected, given that thrusts are active over longer mean
484 times, and they channel material toward the décollement more efficiently, in wedges with stronger décollement or
485 increased sedimentation. While sediments at internal and higher structural positions of the wedge are translated
486 toward the surface and have a lower thermal maturity, sediments at external and lower structural positions are
487 translated toward the décollement and have a relatively higher maturity. The entire cycle is repeated with the
488 formation of new in-sequence thrust.

489 This is a relevant observation for it typifies the causality of particular sediment grains following a high or low
490 maturity path, a long-standing unanswered question (Miyakawa et al., 2019). We corroborate this observation by
491 analyzing the terminal thermal maturity of sediments across a frontal thrust active at a younger age. An example in
492 Fig. 7 shows the thermal maturity of sediments at ~7.5 Myr across a thrust active at ~4 Myr. Whereas this occurs

493 for all thrusts in the wedge, the frontal thrust is particularly pronounced in partitioning sediments into the high and
494 low maturity paths. Thermal maturity correlates with sediment depth weakly near faults and more strongly away
495 from them. The distance of sediment from the frontal thrust dictates the trajectory of sediment grains, and as a
496 result, the pressure-temperature conditions to which they are exposed.

497 Our results show the need to consider all factors influencing fault frequency when inferring the geothermal history
498 of contractional terrains by means of thermal maturity. In this study, we have considered solely how décollement
499 strength and the rate of trench sedimentation vary the frequency, architecture, and overall behavior of thrusts, and
500 the frontal thrust, as the wedge evolves. Fortunately, this predictive exercise should be relatively straightforward,
501 for the impact of these external factors on the fault structure of wedges has been established (Fillon et al., 2012;
502 Mannu et al., 2016, 2017; Mugnier et al., 1997; Simpson, 2010; Storti and McClay, 1995), and the effect of each of
503 these factors can be accounted for when assessing the trajectory of sediments and the distribution of thermal
504 maturity in accretionary wedges. It is nevertheless important to note that the frequency of faults in a wedge can be
505 impacted by many other factors, including hinterland sedimentation (Storti and McClay, 1995; Simpson, 2010;
506 Fernández-Blanco et al. 2020), erosion (Konstantinovskaia, 2005; Willett, 1992), and seafloor topography
507 (Dominguez et al., 2000).

508 ***5.2. Implications of thermal maturity evolution in a subduction wedge***

509 The main implications of this contribution emerge from its predictive power. Our approach can predict to a precise
510 degree the thermal maturity of sediments and the uncertainty associated with the maximum exposure temperature
511 in accretionary contexts with known structuration. A more accurate quantification of the thermal evolution and
512 thermal state of accreted sediments reduces the uncertainties attached to the location of temperature-led
513 transformations of organic material into hydrocarbons in subduction margins and other accretionary contexts. Such

514 increased accuracy in the distribution of thermally mature sediments may also be applied for improved assessments
515 of the evolution in time of any other geothermal process, including seismic slip, magmatic and metamorphic extent,
516 porosity, compaction, and diagenesis of sediments, and the reconstruction of convergent margins in general
517 (Bostick and Pawlewicz, 1984; Mählmann and Le Bayon, 2016; Rabinowitz et al., 2020; Sakaguchi et al., 2011;
518 Totten and Blatt, 1993; Underwood et al., 1992).

519 Our simulations also imply that the paleo-thermal information stored in the incoming sediments can only be
520 retrieved if sediments are at appropriate locations with respect to emergent thrusts. We illustrate this using two runs
521 of the same model and tracking an artificial thermal anomaly imposed on incoming sediments at two different
522 locations (Fig. 8). This hypothetical thermal anomaly can be conceptualized as any alteration of the thermal
523 maturity profile of incoming sediments, for example, elevated heat flows by an antecedent magmatic intrusion.
524 While the change in %Ro associated with the short-lived thermal anomaly results in abnormally high values of
525 thermal maturity in both sediment packages, it can only be retrieved for the end-model run of sediments located
526 further from the trench (those in the right panel, Fig. 8B). Contrarily, the end-model run of sediments closer to the
527 trench (those in the left panel, Fig. 8A) shows no signs of discontinuity in the thermal maturity distribution of the
528 wedge. This is because we deliberately placed the thermal anomaly at sites that evolve at two structural locations
529 during the model run, i.e., above and below a yet-undeveloped frontal thrust (Fig. 8). The sediment sector affected
530 by the thermal anomaly closer to the trench is overthrust by the frontal thrust and remains in a footwall location
531 thereafter (Fig. 8a). In contrast, the homologous sedimentary package further away from the trench is accreted by
532 the frontal thrust and remains in a hanging-wall location (Fig. 8b). Thus, the preservation of the record of an
533 antecedent thermal anomaly is only possible in the former case. We further note that, in our simulations, the entire
534 vertical column of sediments records the thermal anomaly, while in nature, the anomaly may affect only sediments

535 at the deeper locations of the sedimentary pile, which are in turn the sediments that most likely to follow a high-
536 maturity path. We thus regard the possibility of retrieving such antecedent geothermal information as minimal.

537 Finally, among the three methods of R_o computation, Easy R_o and Basin R_o are more consistent and well-
538 constrained on a wide range of thermal maturities in comparison to Simple R_o , which seems to be particularly
539 useful for a smaller range of thermal maturity values. This simply illustrates the fact that while Easy R_o and
540 Basin R_o computation deals with several parallel reactions related to the maturity of kerogen (and hence multiple
541 activation energies), Simple R_o is based on best-fitted single activation energy, and hence yields large confidence
542 intervals at the extreme R_o values. Additionally, the inclusion of the higher activation energy reactions in
543 Basin R_o makes it the best-suited formulation for sediments at the deeper and shear zone sediments which usually
544 get saturated using Easy R_o .

545 *5.3 Comparisons to previous numerical studies*

546 The thermomechanical models presented in this study offer a dynamic representation of trajectories within the
547 wedge. Although the averaged trends in thermal structure and sediment trajectories remain consistent, there are
548 short-term dynamic fluctuations near the frontal thrust. These fluctuations contribute to a diverse range of sediment
549 paths along the depth of the incoming sediments. Miyakawa et al. (2019) conducted a similar study, modeling
550 vitrinite reflectance using Simple R_o and a stationary thermal field, which also resulted in an increase in thermal
551 maturity towards the continent and thermal maturity inversions due to thrusting. However, the use of Simple R_o
552 led to premature saturation and the disappearance of thermal maturity variations at a shallower depth in their model.

553 We can compare our findings with other geodynamic models that examine the thermal structure of the wedge,
554 although there are only a limited number of numerical models of thermal maturity in wedges. Pajang et al. (2022)
555 recently investigated the distribution of the brittle-ductile transition in wedges and proposed a region dominated by

556 viscous shear near the backstop, with the wedge core reaching temperatures of 450°C and typically containing
557 forearc basins. Although trench sedimentation in our model does not result in the formation of forearc basins, the
558 overall flattening of the wedge slope and the high vitrinite reflectance in the core align with consistent structures.
559 Moreover, the presence of highly mature sediments in the wedge core suggests compacted sediments with greater
560 strength and higher P-wave velocity. Although empirical studies have shown a strong correlation between V_p and
561 thermal maturity estimates for depths of up to 4 km (Baig et al, 2016, Mallick et al. 1995), the exact nature of this
562 correlation may vary depending on the specific location. Nevertheless, the patterns of thermal maturity values in
563 the wedge core in our models also correspond to the patterns of P-wave velocity observed in the Nankai and
564 Hikurangi margins (Górszczyk et al., 2019; Nakanishi et al., 2018; Dewing and Sanei, 2009; Arai et al., 2020).

565 Two modes of sediment trajectory evolution, from incoming sediment to their position inside the wedge, are
566 generally considered; depth dependence sediment trajectories, as observed in studies by Mulugeta and Koyi, (1992)
567 and Hori and Sakaguchi (2011), and crossover exhumation pathways, as illustrated by Konstantinovskaia et al.
568 (2005) and Miyakawa (2019). We consider the latter as non-stationary sediment trajectories that vary with time
569 and cut across sediment trajectories of sediments previously located at the same spatial position. Our models show
570 that both modes of sediment trajectories are valid, and that changes in trajectory patterns leading to path crossovers
571 are controlled by the horizontal distance of sediments from the frontal thrust. Starting at a threshold distance from
572 the trench, sediments at different depths follow laminar paths along different trajectories within the wedge.
573 Laminar-type trajectories can be reproduced in a broad range of simulations and are particularly common in models
574 with low sedimentation and décollement strengths. However, the depth dependence of sedimentary paths varies
575 periodically as a function of distance from the trench of specific sedimentary packages (Fig. 5). This effect, which
576 is particularly marked in the neighbourhood of the frontal thrust, explains the crossover paths for incoming
577 sedimentary packages at similar depths but different horizontal locations (Konstantinovskaia et al. 2005).

578 Therefore, thrust faults in the wedge act as the primary agent controlling whether sediments sustain depth-
579 controlled laminar flow or sediment mixing.

580 **5.4 Comparisons to natural wedges**

581 Our models achieve thermal maturity distributions that are in good agreement with their natural analogues, despite
582 several relevant assumptions. Our models are very simplified with regard to their natural analogues, with
583 assumptions such as no elasticity, predefined décollement, no erosion, and simple and uniform rheology. Also, our
584 models have an insufficient resolution for small-scale fault activity and lack empirical relations to simulate the
585 compaction of sediments and multiscale fluid flow. Although these assumptions hinder a wholesale comparison
586 between our simulations and natural examples of accretionary wedges, we still find an acceptable agreement
587 between our model and natural observations, primarily due to simulations that have a temperature evolution
588 assimilating empirical data and a fine spatiotemporal resolution. Our estimated % R_o values for the model are in
589 very good agreement with those measured for the borehole C0002 Nankai accretionary wedge by Fukuchi et al.
590 2009 (Fig. 9). The maximum exposure temperature estimated from the observed thermal maturity for the C0002
591 borehole also strongly correlates with maximum temperatures recorded on markers in the model with similar
592 thermal maturity with 95% confidence (Fig. S17). However, our result is reliant on the empirical thermal
593 conductivity profiles estimated for the C0002 borehole, which does not show any large thermal discontinuity
594 between the forearc basin and inner wedge that has been observed in fossil accretionary wedges (e.g., Underwood
595 et al. 1989).

596 Landward increase in thermal maturity is well documented in studies of the Japan trench, at the Miura–Boso plate
597 subduction margin, the fold and thrust belts Western Foothills complex in western Taiwan, the Mesozoic
598 accretionary prism in the Franciscan subduction complex in northern California, as well as Cretaceous Shimanto
599 accretionary complex in Nankai subduction margin (Yamamoto et al. 2017; Sakaguchi et al. 2007; Underwood et

600 al, 1989; Sakaguchi, 1999). The natural wedges mentioned above display vitrinite reflectance values with
601 maximum %R_o values ranging from 0.2 to 4.0 near the surface, which is generally much higher than the near-
602 surface %R_o values observed in our models. Underwood et al. (1989) suggested that this discrepancy is likely due
603 to the ongoing process of progressive exhumation and erosion, leading to the exposure of deeper sections of the
604 accretionary prism over time. As a result, younger wedges, such as those found in the Miura–Boso plate subduction
605 margin, exhibit a much closer resemblance to the %R_o values near the surface of our our models.

606 On-fault increases in vitrinite reflectance are well also documented in nature, as for boreholes C0004 and C0007,
607 which sample the megasplay fault in Nankai accretionary margin (Sakaguchi et al., 2011). The vitrinite reflectance
608 data from the megasplay and frontal thrusts in Nankai indicate the faults reach a temperature well in excess of
609 300°C during an earthquake, much larger than the background thermal field. Therefore, on-fault increases in
610 thermal maturity are comparatively smaller in our simulations and lack the marked increase in %R_o observed at
611 fault sites in nature. We consider this is due to a discrepancy in the rate of change of thermal diffusion occurring
612 in simulated thrusts, given that our models develop much wider fault zones than their natural equivalents. For
613 instance, the location of megasplay fault in C0007 borehole exhibits an unevenness within the high-reflectance
614 zone with a maximum %R_o ~1.9 (Sakaguchi et al., 2011). This is in line with the prediction by Fulton and Harris
615 (2012) about the impact of fault thickness on change in vitrinite reflectance. Natural observations also exhibit a
616 much higher incidence of on-fault increase in thermal maturity compared to our simulations, given that our models
617 do not have sufficient spatial resolution to capture the large number of thin faults that develop inside the wedge.

618 Natural examples of fault-block inversion have been well-documented in natural settings, providing evidence of
619 past thrust activity preserved in the shallower sections of the Nankai accretionary wedge. Sakaguchi (1999) reported
620 the presence of step increments of thermal maturity, similar to increments in vitrinite reflectance in Fig. 3 and 4
621 across the faults. Other examples are the fault block inversion along the Fukase Fault in the Shimanto accretionary

622 wedge (Ohmori et al., 1997) and the inversion beneath the forearc basin in the Nankai accretionary wedge (Fukuchi
623 et al., 2017).

624 Our study highlights that paleo-thermal anomalies that extend laterally beyond the average thrust spacing have a
625 significantly higher likelihood of being retained in the final thermal maturity record of the wedge. This allows
626 several inferences. For example, the subduction of the Cretaceous ridge, as identified by Underwood et al. (1993)
627 and Sakaguchi (1999), must have caused a substantial alteration in thermal maturity during the Kula-Pacific
628 subduction in order to be discernible in vitrinite reflectance records. Likewise, we can anticipate the preservation
629 of the paleo-thermal anomaly near Ashizuri in the southern Nankai wedge, which has high thrust frequency, in
630 contrast to that at the Muroto transect, where thrust sheets are widely spaced. In the case of the accretionary wedge
631 adjacent to the Boso peninsula, Kamiya et al. (2017) proposed the emplacement of an ophiolite complex beneath
632 the Miura group. Our findings indicate that the preservation of the thermal-advection heating event coincided with
633 a decrease in trench sedimentation. This likely led to an increase in the thrust frequency, which facilitated the
634 preservation of the thermal-advection heating event in the thermal maturity data.

635 **6. Conclusion**

636 This study demonstrates how contractional faults alter the paths of sediments as they accrete and how this
637 fundamentally controls the distribution of the thermal maturity of sediments in accretionary wedges and emphasizes
638 the role that sedimentation rate and interplate contact strength have in such distribution. The increased resolution
639 of our approach leads to findings that have relevant implications. For example, the geothermal history that can be
640 retrieved from the thermal maturity of sediments in drills, i.e., at the shallow wedge, provides, at best, an incomplete
641 record that is skewed towards the thermal evolution of sediments near the trench. Coevally, relevant sectors of
642 sediments located further seaward, when not subducted, follow high-maturity paths that overprint their antecedent

643 thermal history. Finally, this study also provides a first-order uncertainty measure for the thermal maturity of
644 sediments based on the diversity in their trajectory.

645

646 **Code/Data availability**

647 I2VIS, vitrinite reflection computation and visualization codes would be made available by the corresponding
648 author on request.

649 **Author contribution**

650 UM was responsible for the conceptualization of the work, original draft writing, and administration of the paper.
651 DFB contributed to figure visualization, writing and review of the paper. MK and AM contributed to
652 conceptualization and review. TG provided the I2VIS code and contributed to the review of the paper.

653

654 **Acknowledgments**

655 The authors want to acknowledge the topic editor Susanne Buiter as well as the reviewers Jonas B. Ruh and David
656 Hindle for constructive and intriguing reviews and feedback on the original and revised manuscript.

657 **Competing interests**

658 The authors declare that they have no conflict of interest.

659 **References**

660 1. Akuhara, T. (2018). Receiver Function Image of the Subducting Philippine Sea Plate. Fluid Distribution Along the
661 Nankai-Trough Megathrust Fault off the Kii Peninsula: Inferred from Receiver Function Analysis, 43-64.

662 [4-2](#). Arai, R., Kodaira, S., Henrys, S., Bangs, N., Obana, K., Fujie, G., ... & NZ3D Team. (2020). Three-dimensional P
663 wave velocity structure of the Northern Hikurangi margin from the NZ3D experiment: Evidence for fault-bound
664 anisotropy. *Journal of Geophysical Research: Solid Earth*, 125(12), e2020JB020433.

665 [2-3](#). Baig, I., Faleide, J. I., Jahren, J., & Mondol, N. H. (2016). Cenozoic exhumation on the southwestern Barents Shelf:
666 Estimates and uncertainties constrained from compaction and thermal maturity analyses. *Marine and Petroleum*
667 *Geology*, 73, 105-130.

668 [3-4](#). Bostick, N. H., & Pawlewicz, M. J. (1984). Paleotemperatures based on vitrinite reflectance of shales and limestone
669 in igneous dike aureoles in the Upper Cretaceous Pierre shale, Walsenburg, Colorado.

670 [4-5](#). Burnham, A. K., & Sweeney, J. J. (1989). A chemical kinetic model of vitrinite maturation and reflectance. *Geo-*
671 *chimica et Cosmochimica Acta*, 53(10), 2649-2657.

672 [5-6](#). Chi, W. C., & Reed, D. L. (2008). Evolution of shallow, crustal thermal structure from subduction to collision: An
673 example from Taiwan. *Geological Society of America Bulletin*, 120(5-6), 679-690.

674 [6-7](#). Clauser, C., & Huenges, E. (1995). Thermal conductivity of rocks and minerals. *Rock physics and phase relations:*
675 *a handbook of physical constants*, 3, 105-126.

676 [7-8](#). Davis, D., Suppe, J., & Dahlen, F. A. (1983). Mechanics of fold-and-thrust belts and accretionary wedges. *Journal*
677 *of Geophysical Research: Solid Earth*, 88(B2), 1153-1172.

678 [8-9](#). DeMets, C., Gordon, R. G., & Argus, D. F. (2010). Geologically current plate motions. *Geophysical journal inter-*
679 *national*, 181(1), 1-80.

680 [9-10](#). Dewing, K., & Sanei, H. (2009). Analysis of large thermal maturity datasets: Examples from the Canadian
681 Arctic Islands. *International Journal of Coal Geology*, 77(3-4), 436-448.

682 [10-11](#). Dominguez, Stephane, Jacques Malavieille, and Serge E. Lallemand. "Deformation of accretionary wedges
683 in response to seamount subduction: Insights from sandbox experiments." *Tectonics* 19.1 (2000): 182-196.

684 [11-12](#). Fernández-Blanco, D., Mannu, U., Cassola, T., Bertotti G., & Willett SD (2020). Sedimentation and vis-
685 cosity controls on forearc high growth. *Basin Research*, <https://doi.org/10.1111/bre.12518>

686 ~~12-13.~~ Fillon, C., & van der Beek, P. (2012). Post-orogenic evolution of the southern Pyrenees: Constraints from
687 inverse thermo-kinematic modelling of low-temperature thermochronology data. *Basin Research*, 24(4), 418-436.

688 ~~13-14.~~ Fukuchi, M., Nii, T., Ishimaru, N., Minamino, A., Hara, D., Takasaki, I., ... & Tsuda, M. (2009). Valproic
689 acid induces up-or down-regulation of gene expression responsible for the neuronal excitation and inhibition in rat
690 cortical neurons through its epigenetic actions. *Neuroscience research*, 65(1), 35-43.

691 ~~14-15.~~ Fukuchi, R., Yamaguchi, A., Yamamoto, Y., & Ashi, J. (2017). Paleothermal structure of the Nankai inner
692 accretionary wedge estimated from vitrinite reflectance of cuttings. *Geochemistry, Geophysics, Geosystems*, 18(8),
693 3185-3196.

694 ~~15-16.~~ Gerya, T. V., & Yuen, D. A. (2003). Characteristics-based marker-in-cell method with conservative finite-
695 differences schemes for modeling geological flows with strongly variable transport properties. *Physics of the Earth
696 and Planetary Interiors*, 140(4), 293-318.

697 ~~16-17.~~ Gerya, T. V., & Yuen, D. A. (2003). Rayleigh–Taylor instabilities from hydration and melting propel ‘cold
698 plumes’ at subduction zones. *Earth and Planetary Science Letters*, 212(1-2), 47-62.

699 18. Gerya, T. V., & Meilick, F. I. (2011). Geodynamic regimes of subduction under an active margin: effects of rheo-
700 logical weakening by fluids and melts. *Journal of Metamorphic Geology*, 29(1), 7-31.

701 ~~17-19.~~ Górszczyk, A., Operto, S., Schenini, L., & Yamada, Y. (2019). Crustal-scale depth imaging via joint full-
702 waveform inversion of ocean-bottom seismometer data and pre-stack depth migration of multichannel seismic data:
703 a case study from the eastern Nankai Trough. *Solid Earth*, 10(3), 765-784.

704 20. Gool, J. A. V., & Cawood, P. A. (1994). Frontal vs. basal accretion and contrasting particle paths in metamorphic
705 thrust belts. *Geology*, 22(1), 51-54.

706 ~~18-21.~~ Heki, K., Miyazaki, S. I., Takahashi, H., Kasahara, M., Kimata, F., Miura, S., ... & An, K. D. (1999). The
707 Amurian Plate motion and current plate kinematics in eastern Asia. *Journal of Geophysical Research: Solid Earth*,
708 104(B12), 29147-29155.

709 ~~19-22.~~ Henrys, S. A., Ellis, S., & Uruski, C. (2003). Conductive heat flow variations from bottom-simulating re-
710 flectors on the Hikurangi margin, New Zealand. *Geophysical Research Letters*, 30(2).

711 [23.](#) [Hickman, S., Sibson, R., & Bruhn, R. \(1995\). Introduction to special section: Mechanical involvement of fluids in](#)
712 [faulting. *Journal of Geophysical Research: Solid Earth*, 100\(B7\), 12831-12840.](#)

713 [20-24.](#) [Hori, T., & Sakaguchi, H. \(2011\). Mechanism of décollement formation in subduction zones. *Geophysical*
714 \[Journal International\]\(#\), 187\(3\), 1089-1100.](#)

715 [21-25.](#) [Kamiya, N., Yamamoto, Y., Wang, Q., Kurimoto, Y., Zhang, F., & Takemura, T. \(2017\). Major variations](#)
716 [in vitrinite reflectance and consolidation characteristics within a post-middle Miocene forearc basin, central Japan:](#)
717 [A geodynamical implication for basin evolution. *Tectonophysics*, 710, 69-80.](#)

718 [22-26.](#) [Kimura, G., Hashimoto, Y., Kitamura, Y., Yamaguchi, A., & Koge, H. \(2014\). Middle Miocene swift mi-](#)
719 [gration of the TTT triple junction and rapid crustal growth in southwest Japan: A review. *Tectonics*, 33\(7\), 1219-](#)
720 [1238.](#)

721 [23-27.](#) [Konstantinovskaia, E., & Malavieille, J. \(2005\). Erosion and exhumation in accretionary orogens: Experi-](#)
722 [mental and geological approaches. *Geochemistry, Geophysics, Geosystems*, 6\(2\).](#)

723 [24-28.](#) [Konstantinovskaya, E., & Malavieille, J. \(2011\). Thrust wedges with décollement levels and syntectonic](#)
724 [erosion: A view from analog models. *Tectonophysics*, 502\(3-4\), 336-350.](#)

725 [25-29.](#) [Korup, O., Hayakawa, Y., Codilean, A. T., Matsushi, Y., Saito, H., Oguchi, T., & Matsuzaki, H. \(2014\).](#)
726 [Japan's sediment flux to the Pacific Ocean revisited. *Earth-Science Reviews*, 135, 1-16.](#)

727 [26-30.](#) [Lin, W., Fulton, P. M., Harris, R. N., Tadaï, O., Matsubayashi, O., Tanikawa, W., & Kinoshita, M. \(2014\).](#)
728 [Thermal conductivities, thermal diffusivities, and volumetric heat capacities of core samples obtained from the Ja-](#)
729 [pan Trench Fast Drilling Project \(JFAST\). *Earth, Planets and Space*, 66\(1\), 1-11.](#)

730 [27-31.](#) [Maehlmann, R. F., & Le Bayon, R. \(2016\). Vitrinite and vitrinite like solid bitumen reflectance in thermal](#)
731 [maturity studies: Correlations from diagenesis to incipient metamorphism in different geodynamic settings. *Interna-*](#)
732 [tional Journal of Coal Geology](#), 157, 52-73.

733 [28-32.](#) [Malavieille, J., & Trullenque, G. \(2009\). Consequences of continental subduction on forearc basin and](#)
734 [accretionary wedge deformation in SE Taiwan: Insights from analogue modeling. *Tectonophysics*, 466\(3-4\), 377-](#)
735 [394.](#)

736 [29-33.](#) Mallick, R. K., & Raju, S. V. (1995). Thermal maturity evaluation by sonic log and seismic velocity analy-
737 sis in parts of Upper Assam Basin, India. *Organic Geochemistry*, 23(10), 871-879.

738 [30-34.](#) Mannu, U., Ueda, K., Willett, S. D., Gerya, T. V., & Strasser, M. (2016). Impact of sedimentation on evo-
739 lution of accretionary wedges: Insights from high-resolution thermomechanical modeling. *Tectonics*, 35(12), 2828-
740 2846.

741 [34-35.](#) Mannu, U., Ueda, K., Willett, S. D., Gerya, T. V., & Strasser, M. (2017). Stratigraphic signatures of fore-
742 arc basin formation mechanisms. *Geochemistry, Geophysics, Geosystems*, 18(6), 2388-2410.

743 [32-36.](#) Menant, A., Angiboust, S., Gerya, T., Lacassin, R., Simoes, M., & Grandin, R. (2020). Transient stripping
744 of subducting slabs controls periodic forearc uplift. *Nature communications*, 11(1), 1823.

745 [33-37.](#) Miyakawa, A., Kinoshita, M., Hamada, Y., & Otsubo, M. (2019). Thermal maturity structures in an accre-
746 tionary wedge by a numerical simulation. *Progress in Earth and Planetary Science*, 6(1), 1-13.

747 [34-38.](#) Mugnier, J. L., Baby, P., Colletta, B., Vinour, P., Bale, P., & Leturmy, P. (1997). Thrust geometry con-
748 trolled by erosion and sedimentation: A view from analogue models. *Geology*, 25(5), 427-430.

749 [35-39.](#) Mulugeta, G., & Koyi, H. (1992). Episodic accretion and strain partitioning in a model sand wedge. *Tecto-*
750 *nophysics*, 202(2-4), 319-333.

751 [36-40.](#) Nakanishi, A., Takahashi, N., Yamamoto, Y., Takahashi, T., Citak, S. O., Nakamura, T., ... & Kaneda, Y.
752 (2018). Three-dimensional plate geometry and P-wave velocity models of the subduction zone in SW Japan: Impli-
753 cations for seismogenesis.

754 [37-41.](#) Nielsen, S. B., Clausen, O. R., & McGregor, E. (2017). basin% Ro: A vitrinite reflectance model derived
755 from basin and laboratory data. *Basin Research*, 29, 515-536.

756 [38-42.](#) Ohmori, K., Taira, A., Tokuyama, H., Sakaguchi, A., Okamura, M., & Aihara, A. (1997). Paleothermal
757 structure of the Shimanto accretionary prism, Shikoku, Japan: Role of an out-of-sequence thrust. *Geology*, 25(4),
758 327-330.

- 759 [39-43.](#) Pajang, S., Khatib, M. M., Heyhat, M., Cubas, N., Bessiere, E., Letouzey, J., ... & Le Pourhiet, L. (2022).
760 The distinct morphologic signature of underplating and seamounts in accretionary prisms, insights from thermome-
761chanical modeling applied to Coastal Iranian Makran. *Tectonophysics*, 845, 229617.
- 762 [40-44.](#) Platt, J. P. (1986). Dynamics of orogenic wedges and the uplift of high-pressure metamorphic rocks. *Geo-*
763 *logical society of America bulletin*, 97(9), 1037-1053.
- 764 [41-45.](#) Rabinowitz, H. S., Savage, H. M., Polissar, P. J., Rowe, C. D., & Kirkpatrick, J. D. (2020). Earthquake slip
765 surfaces identified by biomarker thermal maturity within the 2011 Tohoku-Oki earthquake fault zone. *Nature com-*
766 *munications*, 11(1), 533.
- 767 [46.](#) Ruh, J. B., Kaus, B. J., & Burg, J. P. (2012). Numerical investigation of deformation mechanics in fold-and-thrust
768 belts: Influence of rheology of single and multiple décollements. *Tectonics*, 31(3).
- 769 [47.](#) Ruh, J. B., Gerya, T., & Burg, J. P. (2014). 3D effects of strain vs. velocity weakening on deformation patterns in
770 accretionary wedges. *Tectonophysics*, 615, 122-141.
- 771 [42-48.](#) Ruh, J. B. (2020). Numerical modeling of tectonic underplating in accretionary wedge systems. *Geo-*
772 *sphere*, 16(6), 1385-1407.
- 773 [43-49.](#) Sakaguchi, A. (1999). Thermal maturity in the Shimanto accretionary prism, southwest Japan, with the
774 thermal change of the subducting slab: fluid inclusion and vitrinite reflectance study. *Earth and Planetary Science*
775 *Letters*, 173(1-2), 61-74.
- 776 [44-50.](#) Sakaguchi, A., Chester, F., Curewitz, D., Fabbri, O., Goldsby, D., Kimura, G., ... & Yamaguchi, A. (2011).
777 Seismic slip propagation to the updip end of plate boundary subduction interface faults: Vitrinite reflectance geo-
778 thermometry on Integrated Ocean Drilling Program NanTro SEIZE cores. *Geology*, 39(4), 395-398.
- 779 [51.](#) Schumann, K., Behrmann, J. H., Stipp, M., Yamamoto, Y., Kitamura, Y., & Lempp, C. (2014). Geotechnical be-
780 havior of mudstones from the Shimanto and Boso accretionary complexes, and implications for the Nankai acce-
781 tionary prism. *Earth, planets and space*, 66, 1-16.
- 782 [45-52.](#) Seno, T., Stein, S., & Gripp, A. E. (1993). A model for the motion of the Philippine Sea plate consistent
783 with NUVEL-1 and geological data. *Journal of Geophysical Research: Solid Earth*, 98(B10), 17941-17948.

Formatted: Pattern: Clear

784 [46-53.](#) Simpson, Guy DH. "Formation of accretionary prisms influenced by sediment subduction and supplied by
785 sediments from adjacent continents." *Geology* 38.2 (2010): 131-134.

786 [47-54.](#) Storti, F., & McClay, K. (1995). Influence of syntectonic sedimentation on thrust wedges in analogue mod-
787 els. *Geol*

788 [48-55.](#) Sugihara, T., Kinoshita, M., Araki, E., Kimura, T., Kyo, M., Namba, Y., ... & Thu, M. K. (2014). Re-eval-
789 uation of temperature at the updip limit of locked portion of Nankai megasplay inferred from IODP Site C0002
790 temperature observatory. *Earth, Planets and Space*, 66(1), 1-14.

791 [49-56.](#) Suzuki, N., Matsubayashi, H., & Waples, D. W. (1993). A simpler kinetic model of vitrinite reflectance.
792 *AAPG bulletin*, 77(9), 1502-1508.

793 [50-57.](#) Sweeney, J. J., & Burnham, A. K. (1990). Evaluation of a simple model of vitrinite reflectance based on
794 chemical kinetics. *AAPG bulletin*, 74(10), 1559-1570.

795 [51-58.](#) Tesei, T., Cruciani, F., & Barchi, M. R. (2021). Gravity-driven deepwater fold-and-thrust belts as Critical
796 Coulomb Wedges: Model limitations and the role of friction vs. fluid pressure. *Journal of Structural Geology*, 153,
797 104451.

798 [52-59.](#) Totten, M. W., & Blatt, H. (1993). Alterations in the non-clay-mineral fraction of pelitic rocks across the
799 diagenetic to low-grade metamorphic transition, Ouachita Mountains, Oklahoma and Arkansas. *Journal of Sedi-
800 mentary Research*, 63(5), 899-908.

801 [53-60.](#) Turcotte, D. L., & Schubert, G. (2002). *Geodynamics*. Cambridge university press.

802 [54-61.](#) Underwood, M. B., Moore, G. F., Taira, A., Klaus, A., Wilson, M. E., Fergusson, C. L., ... & Steurer, J.
803 (2003). Sedimentary and tectonic evolution of a trench-slope basin in the Nankai subduction zone of southwest Ja-
804 pan. *Journal of Sedimentary Research*, 73(4), 589-602.

805 [55-62.](#) Underwood, M. B., O'Leary, J. D., & Strong, R. H. (1988). Contrasts in thermal maturity within terranes
806 and across terrane boundaries of the Franciscan Complex, northern California. *The Journal of Geology*, 96(4), 399-
807 415.

808 [56-63.](#) Underwood, M. B. (1989). Temporal changes in geothermal gradient, Franciscan subduction
809 complex, northern California. *Journal of Geophysical Research: Solid Earth*, 94(B3), 3111-3125.

810 [57-64.](#) Wenk, L., & Huhn, K. (2013). The influence of an embedded viscoelastic-plastic layer on kinematics and
811 mass transport pattern within accretionary wedges. *Tectonophysics*, 608, 653-666.

812 [58-65.](#) Willett, S. D. (1992). Dynamic and kinematic growth and change of a Coulomb wedge. In *Thrust tectonics*
813 (pp. 19-31). Dordrecht: Springer Netherlands.

814 [59-66.](#) Yamano, M., Foucher, J. P., Kinoshita, M., Fisher, A., Hyndman, R. D., Leg, O. D. P., & Party, S. S.
815 (1992). Heat flow and fluid flow regime in the western Nankai accretionary prism. *Earth and Planetary Science*
816 *Letters*, 109(3-4), 451-462.

817 [60-67.](#) Zhao, D., Wang, J., Huang, Z., & Liu, X. (2021). Seismic structure and subduction dynamics of the west-
818 ern Japan arc. *Tectonophysics*, 802, 228743.

819

820

821

822

823

824

|825

832 **Table 2: Model runs and their specific characteristic observations**

Models	ϕ_b	ϕ / ϕ_{ss}	λ	<i>SR</i>	<i>L</i>	$\beta(^{\circ})$	$\alpha(^{\circ})$	$\alpha_{predicted}$ (ϕ_{ss} / ϕ) ($^{\circ}$)	<i>D</i>	$\langle R_o \% \rangle$	% <i>top-half</i>	% <i>Bottom-half</i>
$M_0^{4.5}$	4.5 $^{\circ}$	30 $^{\circ}$ /20 $^{\circ}$	0	None	123.2 \pm 15.7	4.2 \pm 0.6	0.95 \pm 0.3	0.03 \pm 0.2/-1.3 \pm 0.3	15.5 \pm 7.0	0.54	0.0	12.7
M_0^7	7 $^{\circ}$	30 $^{\circ}$ /20 $^{\circ}$	0	None	97.7 \pm 9.9	4.9 \pm 0.8	2.6 \pm 0.8	0.97 \pm 0.2/-0.95 \pm 0.3	12.1 \pm 3.6	0.60	0.0	22.5
$M_0^{9.5}$	9.5 $^{\circ}$	30 $^{\circ}$ /20 $^{\circ}$	0	None	77.8 \pm 4.8	5.3 \pm 0.8	3.7 \pm 0.9	2.1 \pm 0.4/-0.32 \pm 0.3	8.7 \pm 2.1	0.67	0.0	31.3
$M_{0.1}^{9.5}$	9.5 $^{\circ}$	30 $^{\circ}$ /20 $^{\circ}$	0	0.1	76.1 \pm 5.9	5.0 \pm 0.9	2.3 \pm 0.7	2.3 \pm 0.4/-0.12 \pm 0.3	7.3 \pm 1.1	0.71	0.1	35.3
$M_{0.3}^{9.5}$	9.5 $^{\circ}$	30 $^{\circ}$ /20 $^{\circ}$	0	0.3	79.3 \pm 8.2	4.9 \pm 0.9	2.0 \pm 0.5	2.3 \pm 0.4/-0.1 \pm 0.3	7.8 \pm 2.5	0.69	0.1	32.0
$M_{0.5}^{9.5}$	9.5 $^{\circ}$	30 $^{\circ}$ /20 $^{\circ}$	0	0.5	79.9 \pm 7.4	4.9 \pm 0.8	2.1 \pm 0.5	2.3 \pm 0.4/-0.1 \pm 0.2	9.5 \pm 4.0	0.71	2.7	34.4
$M_{0.7}^{9.5}$	9.5 $^{\circ}$	30 $^{\circ}$ /20 $^{\circ}$	0	0.7	81.3 \pm 10.5	5.0 \pm 0.9	2.1 \pm 0.5	2.3 \pm 0.7/-0.11 \pm 0.3	9.9 \pm 5.0	0.73	4.2	41.5
$M_{0.9}^{9.5}$	9.5 $^{\circ}$	30 $^{\circ}$ /20 $^{\circ}$	0	0.9	82.5 \pm 11.0	5.0 \pm 0.9	2.3 \pm 0.7	2.2 \pm 0.4/-0.16 \pm 0.3	13.8 \pm 7.8	0.75	14.6	51.8
M_0^{12}	12 $^{\circ}$	30 $^{\circ}$ /20 $^{\circ}$	0	None	71.6 \pm 5.0	5.6 \pm 1.0	5.1 \pm 1.0	3.5 \pm 0.6/0.4 \pm 0.4	8.8 \pm 3.3	0.83	1.2	40.6
$M_0^{14.5}$	14.5 $^{\circ}$	30 $^{\circ}$ /20 $^{\circ}$	0	None	62.7 \pm 6.0	5.9 \pm 1.0	6.7 \pm 1.4	5.1 \pm 0.8/1.2 \pm 0.4	8.0 \pm 1.8	0.94	2.0	54.0

ϕ_b is décollement Strength (internal angle of friction).

ϕ Sediment Strength.

ϕ_{ss} Sediment Strength (Strain weakened)/ (internal angle of friction).

SR Average Sediment rate (mm/yr).

λ is pore-fluid pressure ratio.

L Average Length of the wedge (in km) between ~2.5-7.5Myr. Length of the wedge is computed as the distance between trench and backstop(set at 1850 km from the right edge of the modelling domain).

β Average basal dip angle β (in degrees) between ~2.5-7.5Myr measure by fitting a line in the basal surface.

α Average surface slope angle α (in degrees) between ~2.5-7.5Myr measure computing the slope of fitting the best fitted line in the surface.

D Average Distance between the first and second frontal thrust between ~2.5-7.5Myr (in km). The frontal thrust is always identified from the trench. The send thrust is identified by the high strain rate and deviation of the weak décollement material from the trend of oceanic plate.

$\alpha_{predicted}$ (ϕ_{ss} / ϕ) is the surface slope predicted using critical wedge theory using the β observed in the model and sediment strength (Initial /Strain weakened).

T Average time a frontal thrust remains active between ~3.5-7.5Myr.

$\langle R_o \% \rangle$ Average vitrinite reflectance of the wedge between ~3.5-7.5 Myr.

%*top* Proportion of >1 eventual $R_o\%$ (*vitrinite reflectance at 7.5 Myr*) at shallow half of the incoming sediment at 2.5 Myr.

%*bottom* Proportion of >1 eventual $R_o\%$ (*vitrinite reflectance at 7.5 Myr*) at deep half of the incoming sediments.

*Please see Fig. S18 for details on the various measurement done on the wedge.

834 **Table 3: Parameters for Easy%Ro, Simple%Ro and Basin%Ro vitrinite reflectance model.**

S. No.	Stoichiometric Coefficient for Easy%Ro (x_{0i_Easy})	Activation Energy for Easy%Ro (kJ/mol) (E_{ai_Easy})	Stoichiometric Coefficient for Simple%Ro (x_{0i_Simple})	Activation Energy(E) for Simple%Ro (E_{ai_Simple})	Stoichiometric Coefficient for Simple%Ro (x_{0i_Basin})	Activation Energy(E) for Basin%Ro (kJ/mol) (E_{ai_Simple})
1	0.0300	142256	1	1.38e5	0.0185	142256
2	0.0300	150624	:	:	0.0143	150624
3	0.0400	158992	:	:	0.0569	158992
4	0.0400	167360	:	:	0.0478	167360
5	0.0500	175728	:	:	0.0497	175728
6	0.0500	184096	:	:	0.0344	184096
7	0.0600	192464	:	:	0.0344	192464
8	0.0400	200832	:	:	0.0322	200832
9	0.0400	209200	:	:	0.0282	209200
10	0.0700	217568	:	:	0.0062	217568
11	0.0600	225936	:	:	0.1155	225936
12	0.0600	234304	:	:	0.1041	234304
13	0.0600	242672	:	:	0.1023	242672
14	0.0500	251040	:	:	0.076	251040
15	0.0500	259408	:	:	0.0593	259408
16	0.0400	267776	:	:	0.0512	267776
17	0.0300	276144	:	:	0.0477	276144
18	0.0200	284512	:	:	0.0086	284512
19	0.0200	292880	:	:	0.0246	292880
20	0.0100	301248	:	:	0.0096	301248
A _{Easy} = 1e13 and %R _{o0} = 0.2, A _{Simple} = 1e13 and %R _{o0} = 0.2, A _{Basin} = 9.7029e12 and %R _{o0} = 0.2104						

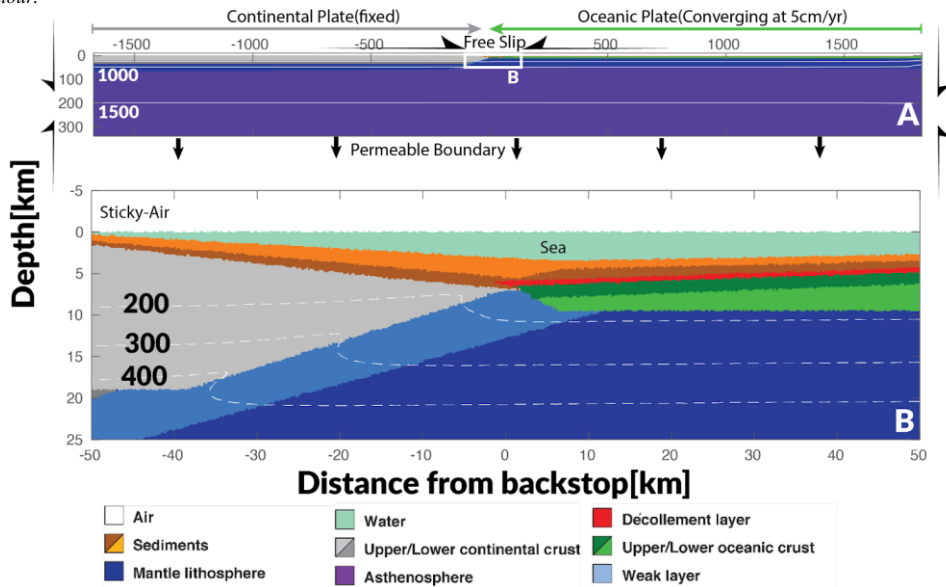
835

836

837 **List of Figures**

838 **Fig. 1:**

839 *Initial model setup. A. The lithological and geothermal map of the whole computational domain with boundary conditions. B.*
 840 *The zoomed lithological and geothermal map of the inset illustrates the junction of continental and oceanic plates. The colors*
 841 *represent different lithology of the materials used in the models, with upper and lower crust represented by light and dark*
 842 *grey, upper and lower oceanic crust represented by dark and light green. The arrows around the computational domain*
 843 *represent the imposed boundary conditions, while the white contour lines (dashed in the zoomed panel) show the geothermal*
 844 *gradients used for the initial model. The numbers on the white contour lines represent the temperature values in °C for the*
 845 *contour.*



846 h

847

848

849

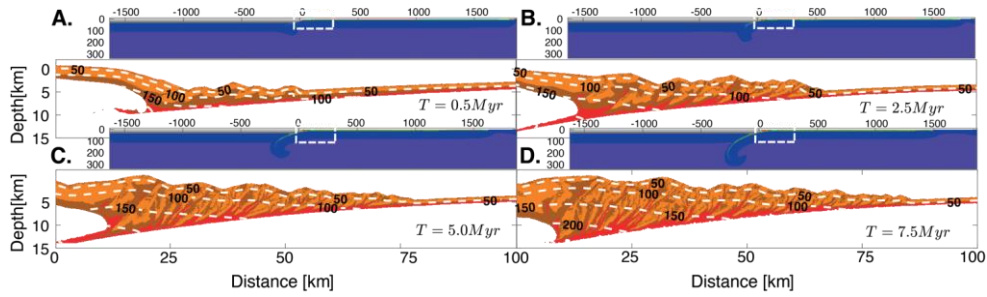
850

851

852

853

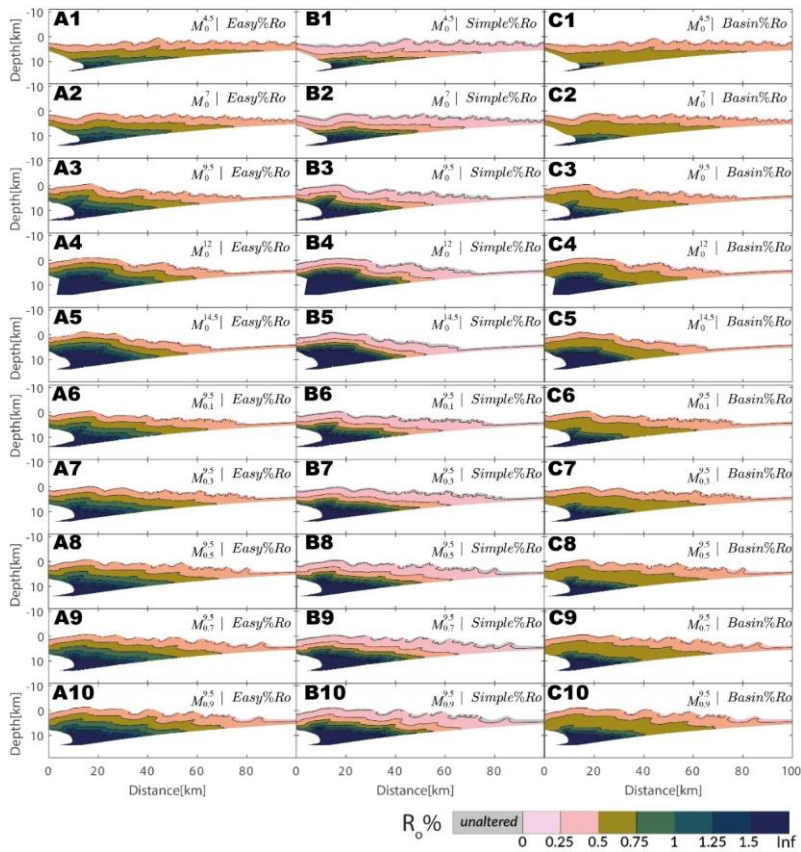
854 **Fig. 2:**
 855 *Typical thermomechanical evolution of the accretionary wedge for model M_0^7 at (a) 0.5*
 856 *Myr (b) 2.5 Myr (c) 5.0 Myr (d) 7.5 Myr. Similar Figures for other models have been illustrated in supplementary images. The*
 857 *colormap for the panels is same as Figure 1.*
 858



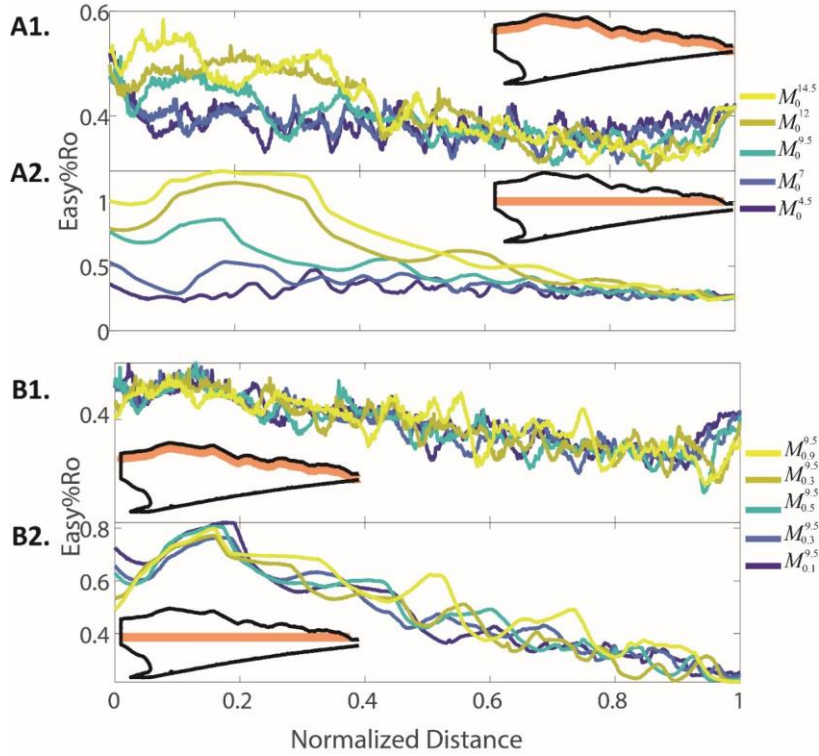
859
 860
 861
 862
 863
 864
 865
 866
 867
 868
 869
 870
 871
 872
 873
 874
 875
 876
 877
 878

879 **Fig. 3:**
 880 *Distribution of thermal maturity for different models at ~6.0 Myr (3.5 Myr of thermal maturation). Panels A1-A5 show the*
 881 *thermal maturity distribution (computed using Easy%Ro) in subduction wedges of models as a function of décollement strength*
 882 *, respectively. A6-A10 show the thermal maturity distribution in subduction wedges of models function of sedimentation rate*
 883 *, respectively. The grey color of the markers indicate that no thermal maturity change in these sediments have not occurred.*
 884 *B1-B10 and C1-C10 similarly show the thermal maturity distribution in subduction wedges computed using Simple%Ro, and*
 885 *Basin%Ro, respectively.*

886

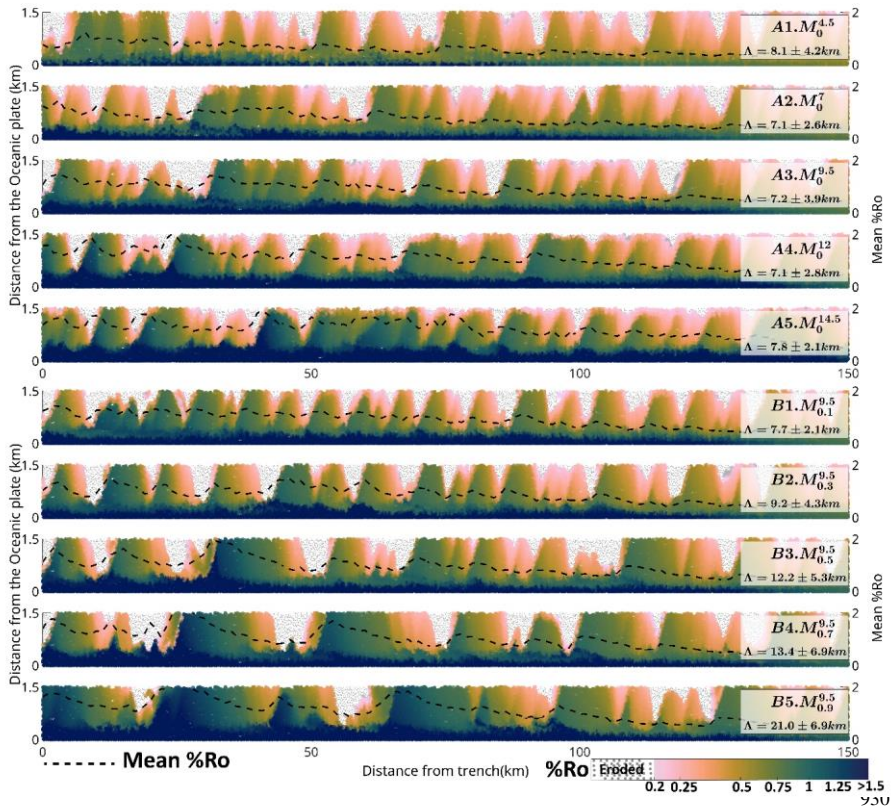


887 **Fig. 4:**
 888 The variation of % R_o for a horizon as indicated by the orange band in the inset at 7.5 Myr. Panel A1 and A2 shows all the
 889 models with different decollement strength. Panel B1 and B2 shows all the models with different sedimentation rates. Horizons
 890 in panel A1 and B1 are located at 1 km depth from the surface, whole in panel A2 and B2 the horizons are horizontal zones
 891 located at the trench depth. The horizontal distance from the backstop is normalized by the wedge length. Horizontal distance
 892 0 represents the fixed backstop and 1 represents the trench.
 893



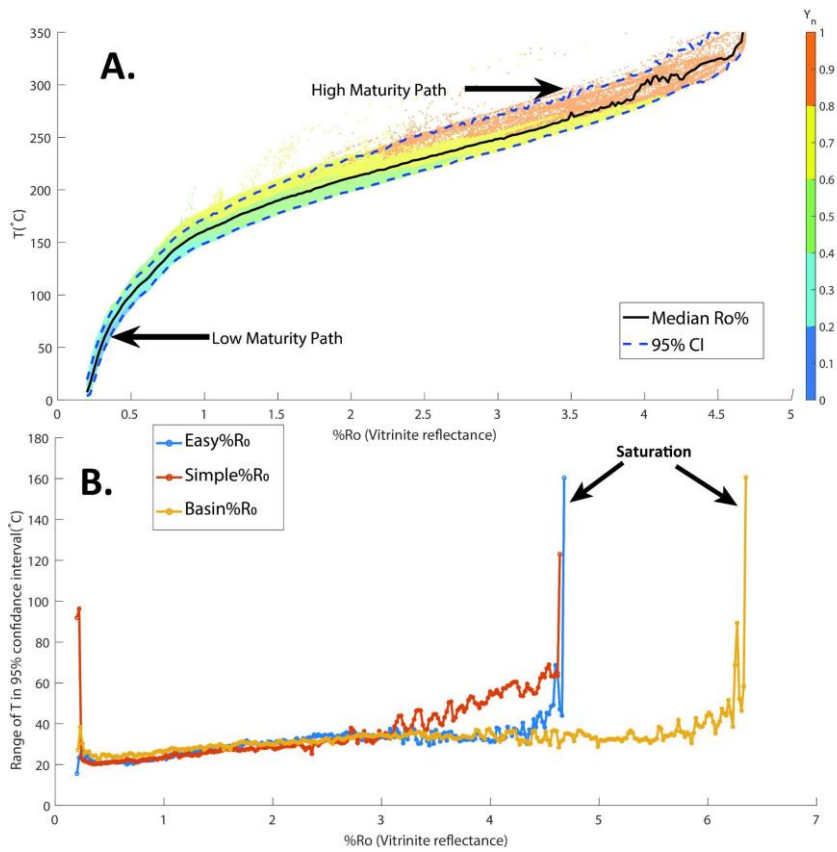
894
 895
 896
 897
 898

899 **Fig. 5:**
 900 *Map of thermal maturity at 7.5 Myr mapped to sediments at 2.5 Myr. Panel A1-A5, B1-B5 show the mapping for models - and*
 901 *- respectively. The vertical axis (distance from the oceanic plate) has been corrected for the bending of the plate. The horizontal*
 902 *axis represents the distance of sediments from the trench. The grey colour of the markers indicates that these sediments have*
 903 *been eroded/reworked due to slope failure. The broken black line represents the mean %R₀ attained sediment at a given*
 904 *distance from the trench. Λ represents the horizontal periodicity in mean %R₀ for the given model.*
 905



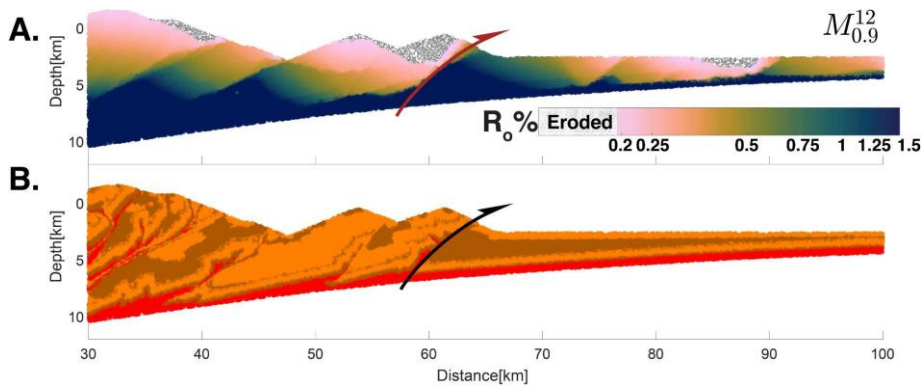
931
 932

933 **Fig. 6:**
 934 A. Vitrinite Reflectance (%Ro) vs Maximum Exposure temperature in all models. The colours in panel A represent the depth
 935 of the sediments at 7.5 Myr normalized by the thickness of the wedge (Y_n). B. Range of 95% CI for Easy%Ro, Simple%Ro and
 936 Basin%Ro. Y_n is the depth of the marker from the surface normalized by the thickness (vertical extent) of the wedge at the
 937 location of the marker. Please see panel B of Fig. S16 for computation of Y_n .
 938



939

940 **Fig. 7:**
941 Mapping of eventual thermal maturity (vitrinite reflectance at 7.5Myr) to the location of same markers at ~4Myr in model .
942 Panel A shows the values of thermal maturity for the markers while the lithology of the wedge is shown in panel B. The half
943 arrow represents the active frontal thrust. The sediments which were eroded by 7.5Myr but exist at 4Myr have been markers
944 eroded using dotted grey points.



945

946

947

948

949

950

951

952

953

954

955

956

957

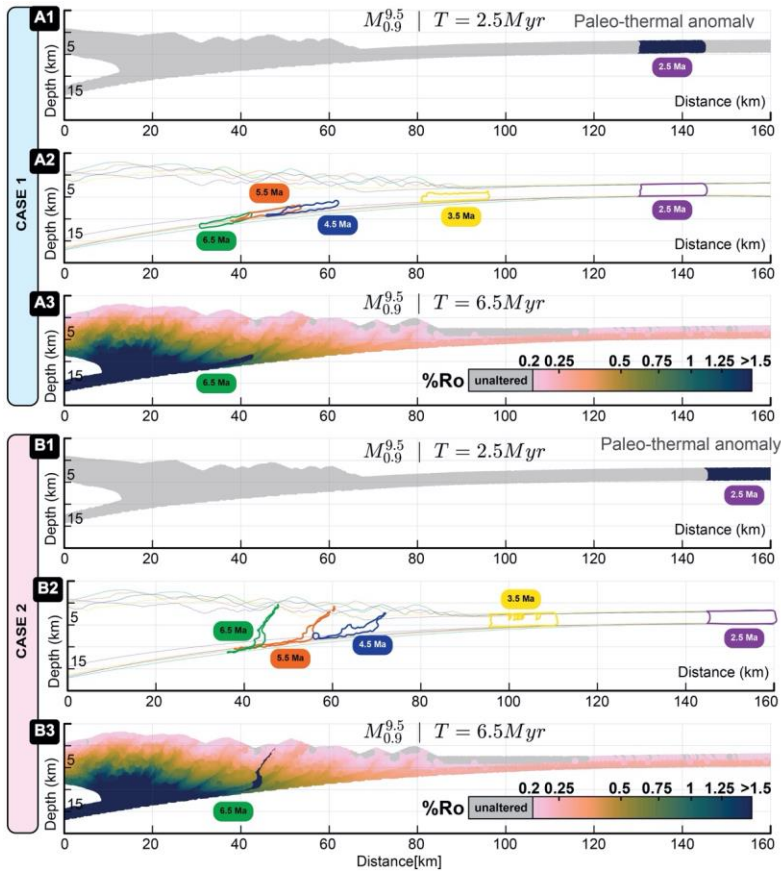
958

959

960

961
962
963
964
965
966
967
968

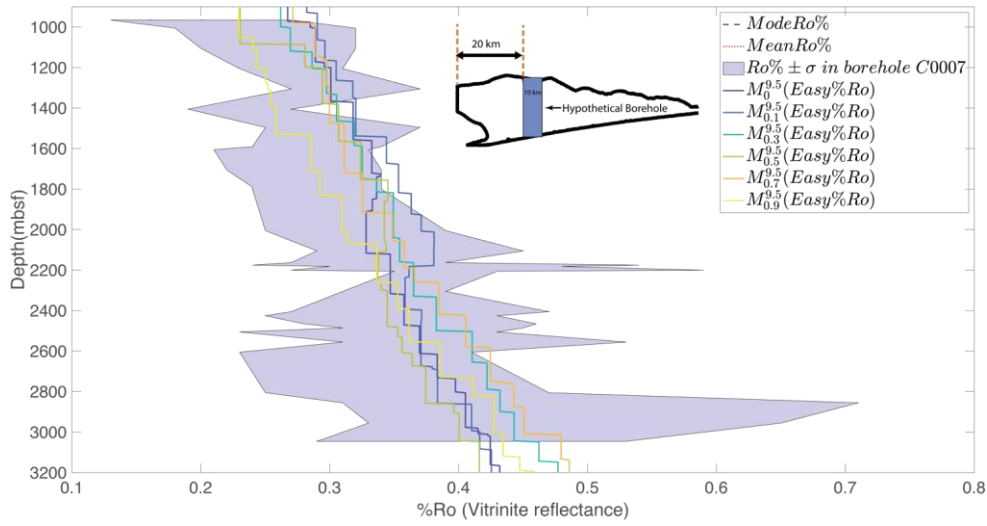
Fig. 8:
Position dependency of thermal maturity preservation. A1. Distribution of %R_o at 2.5 Myr with a paleo-thermal anomaly emplaced at 130-145 km from the backstop. A2. The evolution of the emplaced paleo-thermal anomaly from 2.5 Myr to 6.5 Myr in case 1. A3. Distribution of %R_o at 2.5 Myr. B1. Distribution of %R_o at 2.5 Myr with a paleo-thermal anomaly emplaced at 145-160 km from the backstop. B2. The evolution of the emplaced paleo-thermal anomaly from 2.5 Myr to 6.5 Myr in case 2. B3. Distribution of %R_o at 2.5 Myr with a paleo-thermal anomaly emplaced at 145-160 km from the backstop.



969
970

971
972
973
974
975
976
977

Fig. 9:
Depth vs Thermal maturity (%Ro). The shaded (in violet) region shows the range of observed Ro% (mean±1SD) from the C0002 borehole ,colored lines represent the values in models sampled from a 10 km wide hypothetical borehole 20km seaward of the backstop as shown in the inset .

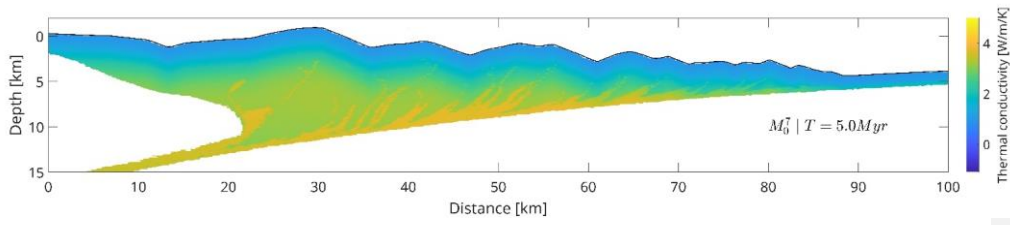


978
979
980
981

982 **Supplementary Figures**

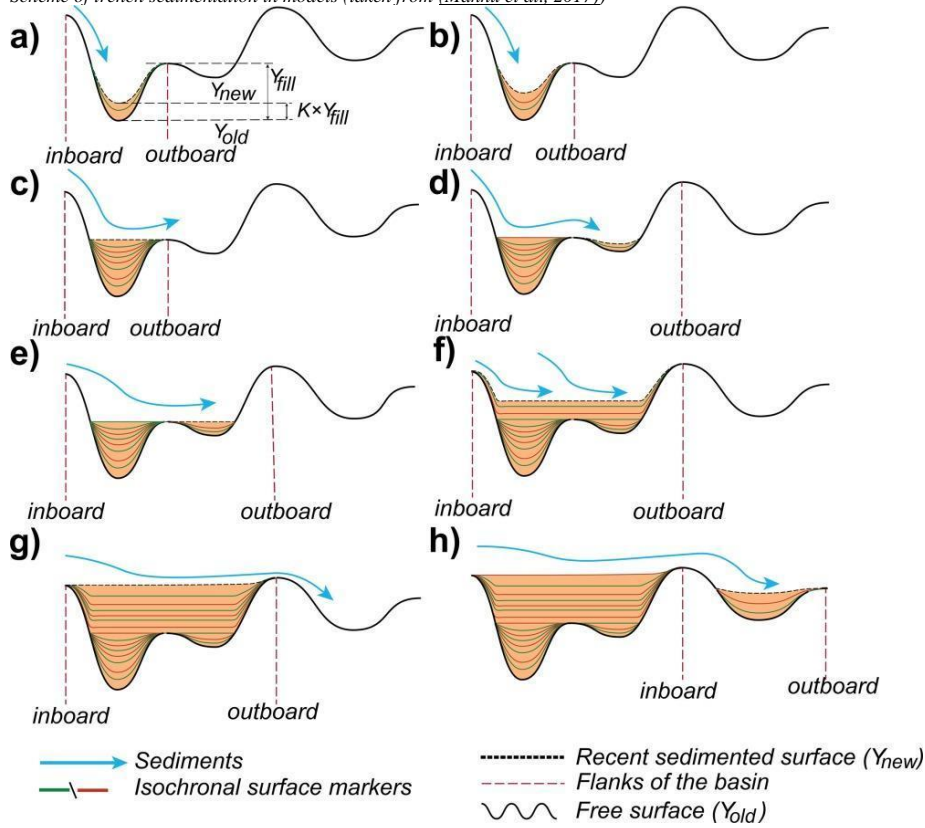
983 **Fig. S1:**

984 *Typical Distribution of thermal conductivity in wedge*



1000 Fig. S2:

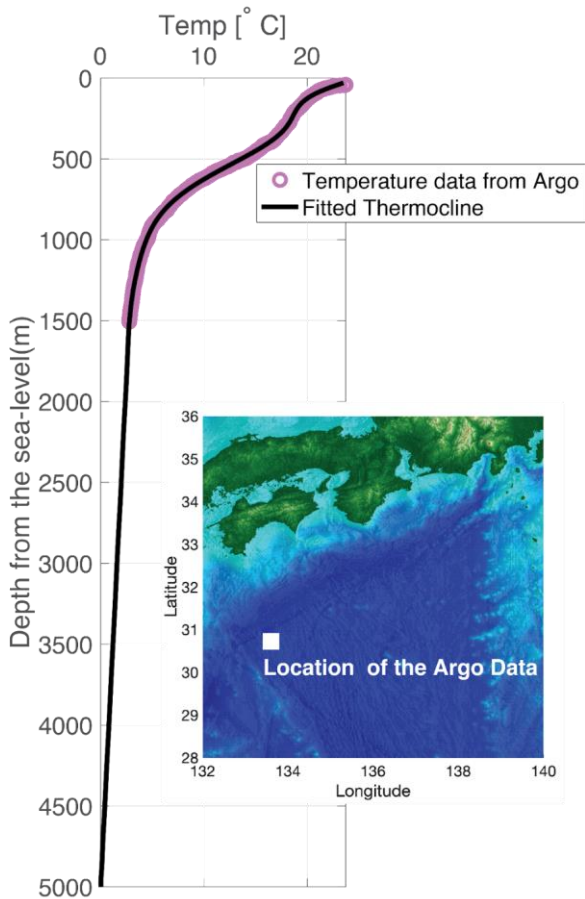
1001 Scheme of trench sedimentation in models (taken from (Mannu et al., 2017))



1002
1003
1004
1005
1006
1007

1008 **Fig. S3:**

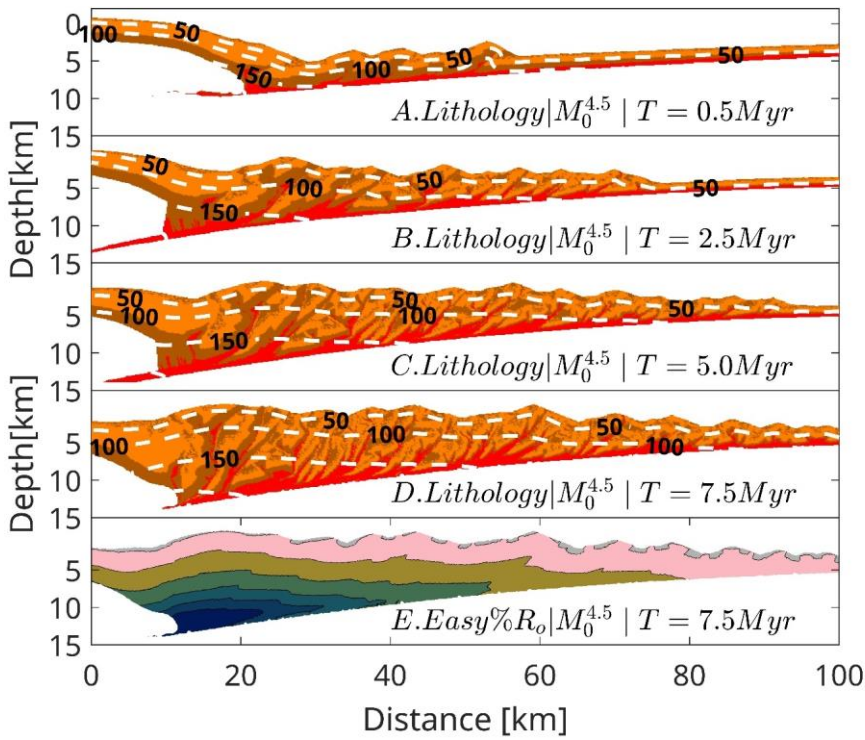
1009 *Plot of Temperature vs Depth profile in for water-sediment interaction using the data from the International Argo Program*
1010 *and the national programs that contribute for the location(represented by the white square) given in the inset The magenta*
1011 *circle represents the Temperature vs Depth profile from the data while the black line is the fitted thermocline used in our*
1012 *models for water-sediment thermal interaction.*
1013



1014

1015 **Fig. S4:**
 1016 Typical thermomechanical evolution of the accretionary wedge for model $M_0^{4.5}$ at 0.5 Myr, 2.5 Myr, 5.0 Myr and 7.5 Myr of
 1017 lithological evolution (Panel A-D). The dashed white lines represent the contours of the temperature field. The colormap for
 1018 the first 4 panels is same as Figure 1. The last panel represents thermal maturity values at ~7.5 Myr computed using Easy% R_o .
 1019 The colormap for Panel E is same as that of Figure 3.

1020



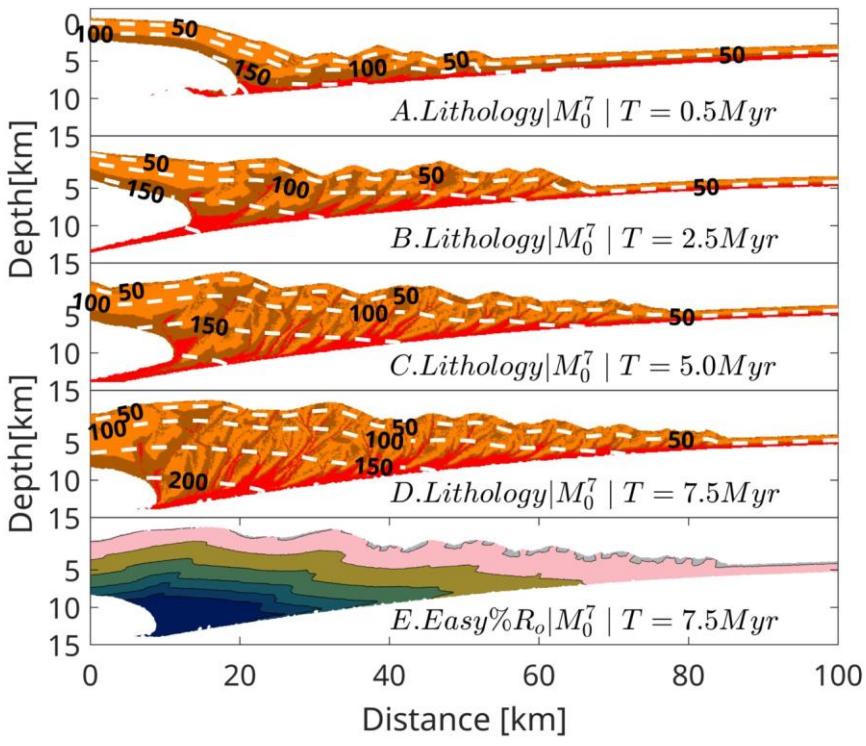
1022

1023

1024

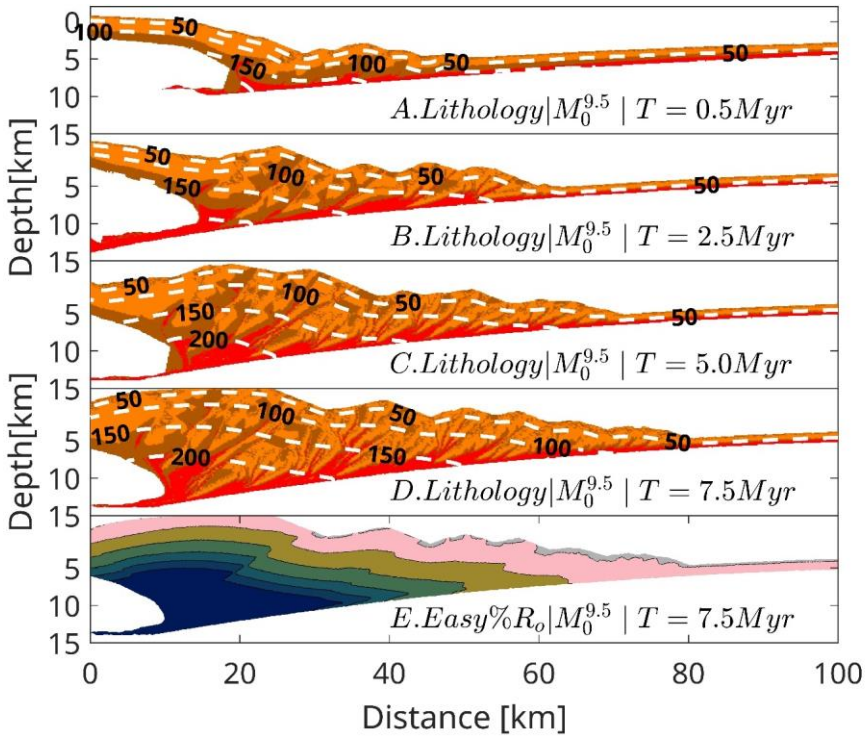
1025

1026 **Fig. S5:**
 1027 Typical thermomechanical evolution of the accretionary wedge for model M_0^7 at 0.5 Myr, 2.5 Myr, 5.0 Myr and 7.5 Myr of
 1028 lithological evolution (Panel A-D). The dashed white lines represent the contours of the temperature field. The colormap for
 1029 the first 4 panels is same as Figure 1. The last panel represents thermal maturity values at ~7.5 Myr computed using Easy% R_o .
 1030 The colormap for Panel E is same as that of Figure 3.
 1031



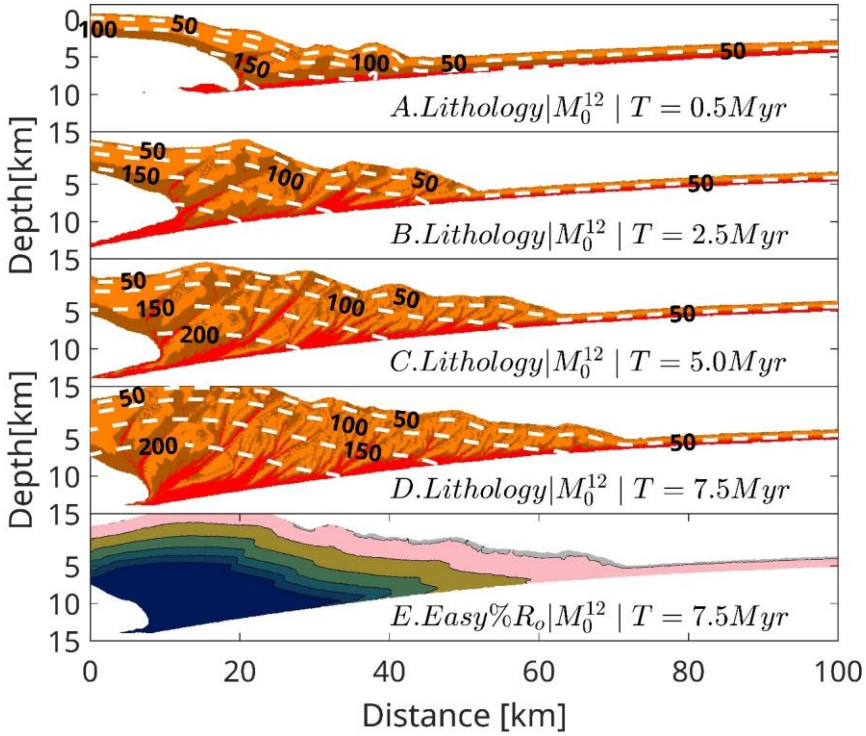
1032
 1033
 1034
 1035
 1036
 1037

1038 **Fig. S6:**
 1039 Typical thermomechanical evolution of the accretionary wedge for model $M_0^{9.5}$ at 0.5 Myr, 2.5 Myr, 5.0 Myr and 7.5 Myr of
 1040 lithological evolution (Panel A-D). The dashed white lines represent the contours of the temperature field. The colormap for
 1041 the first 4 panels is same as Figure 1. The last panel represents thermal maturity values at ~7.5 Myr computed using Easy% R_o .
 1042 The colormap for Panel E is same as that of Figure 3.
 1043
 1044



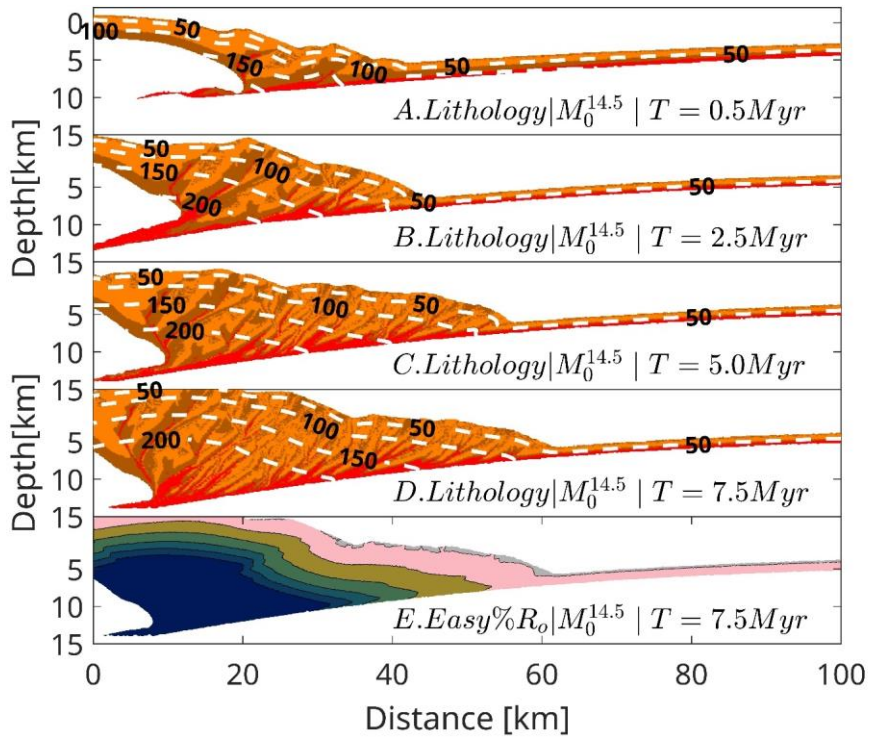
1045
 1046
 1047
 1048
 1049
 1050

1051 **Fig. S7:**
 1052 Typical thermomechanical evolution of the accretionary wedge for model M_0^{12} at 0.5 Myr, 2.5 Myr, 5.0 Myr and 7.5 Myr of
 1053 lithological evolution (Panel A-D). The dashed white lines represent the contours of the temperature field. The colormap for
 1054 the first 4 panels is same as Figure 1. The last panel represents thermal maturity values at ~ 7.5 Myr computed using Easy% R_o .
 1055 The colormap for Panel E is same as that of Figure 3.
 1056
 1057



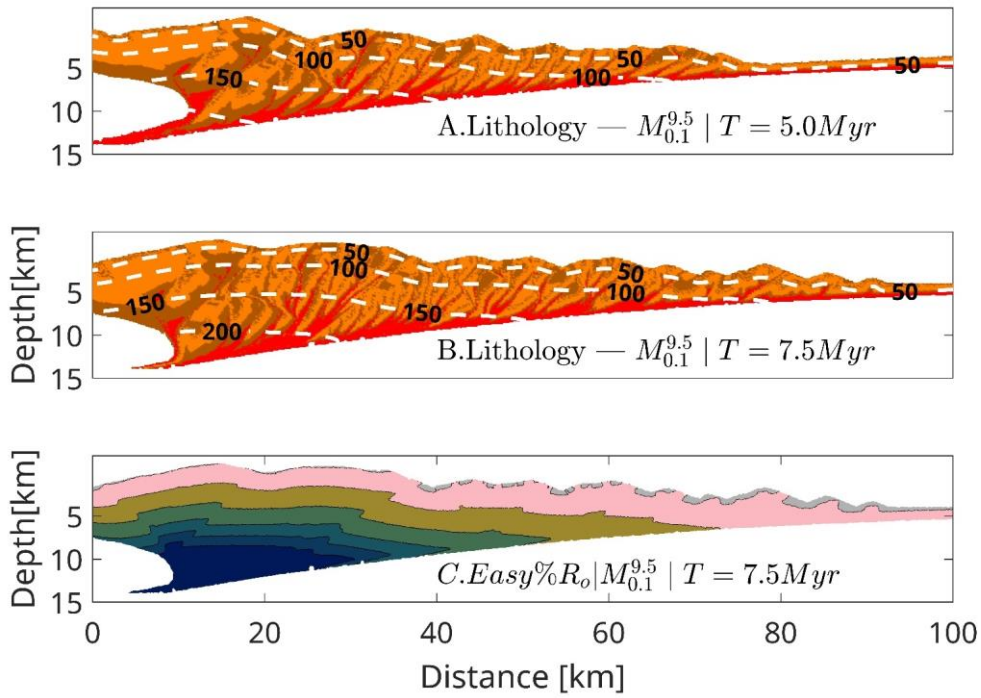
1058
 1059
 1060
 1061
 1062

1063 **Fig. S8:**
 1064 Typical thermomechanical evolution of the accretionary wedge for model $M_0^{14.5}$ at 0.5 Myr, 2.5 Myr, 5.0 Myr and 7.5 Myr of
 1065 lithological evolution (Panel A-D). The dashed white lines represent the contours of the temperature field. The colormap for
 1066 the first 4 panels is same as Figure 1. The last panel represents thermal maturity values at ~7.5 Myr computed using Easy% R_o .
 1067 The colormap for Panel E is same as that of Figure 3.
 1068



1069
 1070
 1071
 1072
 1073

1074 **Fig. S9:**
 1075 Typical thermomechanical evolution of the accretionary wedge for model $M_{0.1}^{9.5}$ at 5.0 Myr and 7.5 Myr of lithological evolution
 1076 (Panel A-B). The dashed white lines represent the contours of the temperature field. The colormap for the first 2 panels is
 1077 same as Figure 1. The Panel C represents thermal maturity values at ~7.5 Myr computed using Easy% R_o . The colormap for
 1078 Panel E is same as that of Figure 3.
 1079
 1080

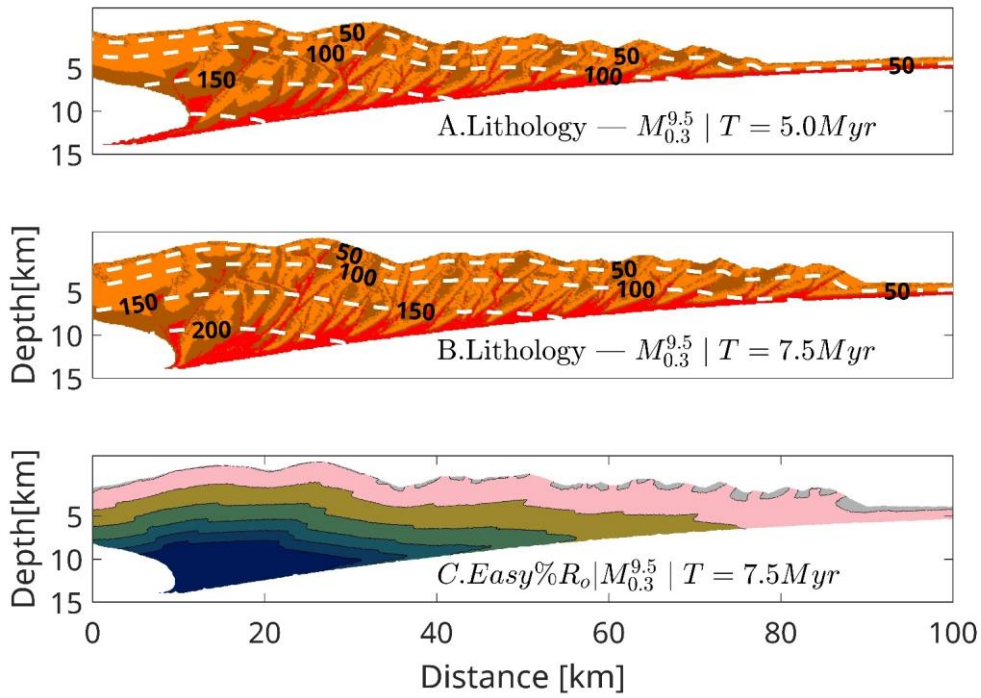


1081
 1082
 1083
 1084
 1085
 1086

1087
1088
1089
1090
1091
1092
1093
1094

Fig. S10:

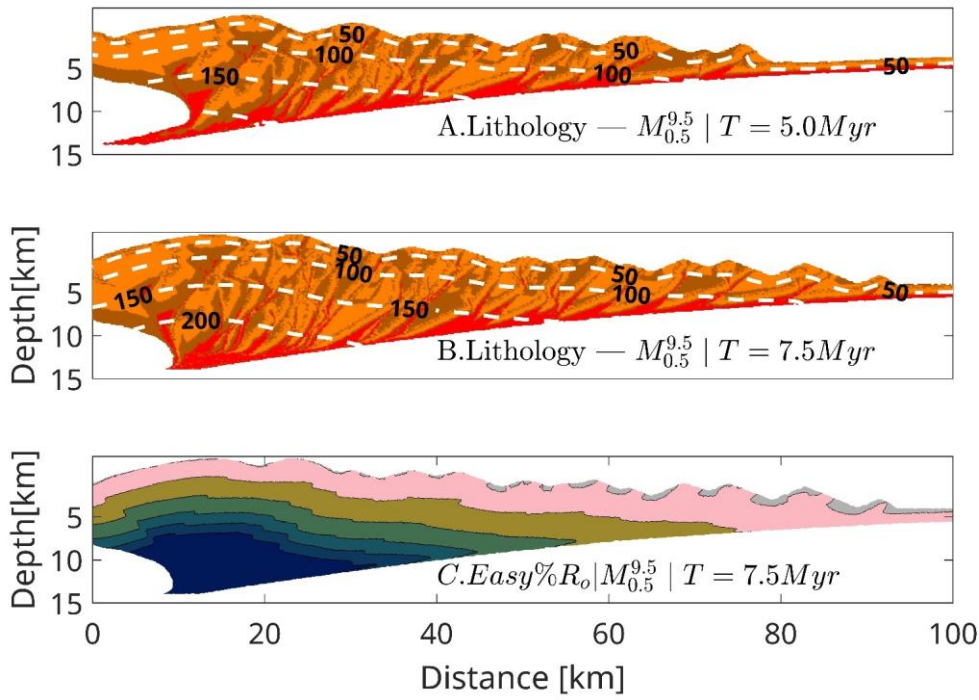
Typical thermomechanical evolution of the accretionary wedge for model $M_{0.3}^{9.5}$ at 5.0 Myr and 7.5 Myr of lithological evolution (Panel A-B). The dashed white lines represent the contours of the temperature field. The colormap for the first 2 panels is same as Figure 1. The Panel C represents thermal maturity values at ~7.5 Myr computed using Easy% R_o . The colormap for Panel E is same as that of Figure 3.



1095
1096
1097
1098
1099

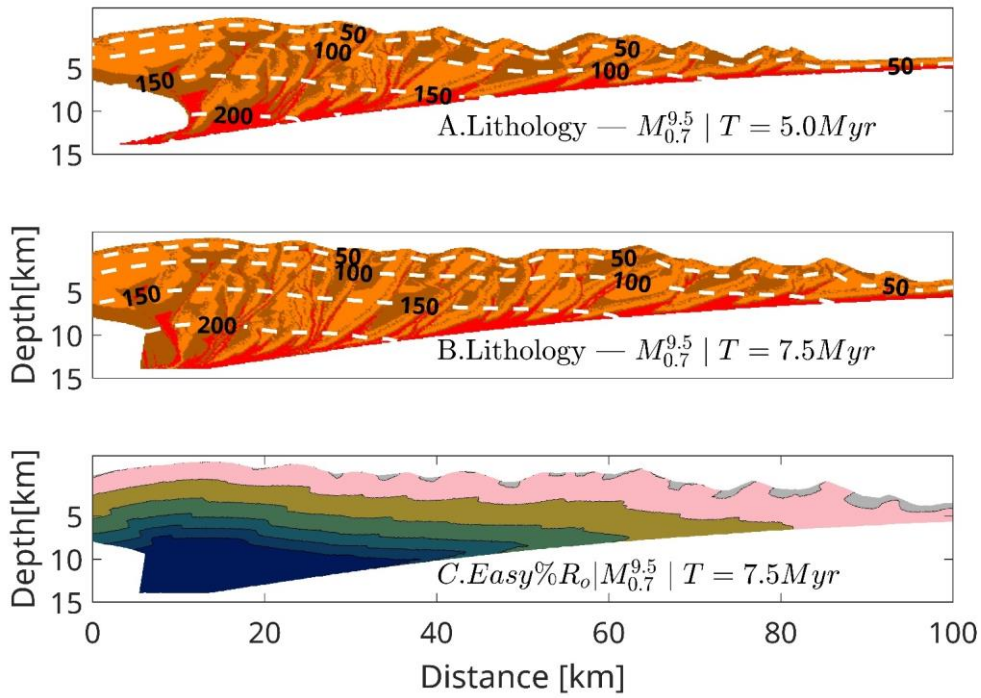
1100
1101
1102
1103
1104
1105
1106
1107

Fig. S11:
Typical thermomechanical evolution of the accretionary wedge for model $M_{0.5}^{4.5}$ at 5.0 Myr and 7.5 Myr of lithological evolution (Panel A-B). The dashed white lines represent the contours of the temperature field. The colormap for the first 2 panels is same as Figure 1. The Panel C represents thermal maturity values at ~ 7.5 Myr computed using Easy% R_o . The colormap for Panel E is same as that of Figure 3.



1108
1109
1110
1111
1112

1113 **Fig. S12:**
 1114 Typical thermomechanical evolution of the accretionary wedge for model $M_{0.7}^{9.5}$ at 5.0 Myr and 7.5 Myr of lithological evolution
 1115 (Panel A-B). The dashed white lines represent the contours of the temperature field. The colormap for the first 2 panels is
 1116 same as Figure 1. The Panel C represents thermal maturity values at ~7.5 Myr computed using Easy%Ro. The colormap for
 1117 Panel E is same as that of Figure 3.
 1118
 1119

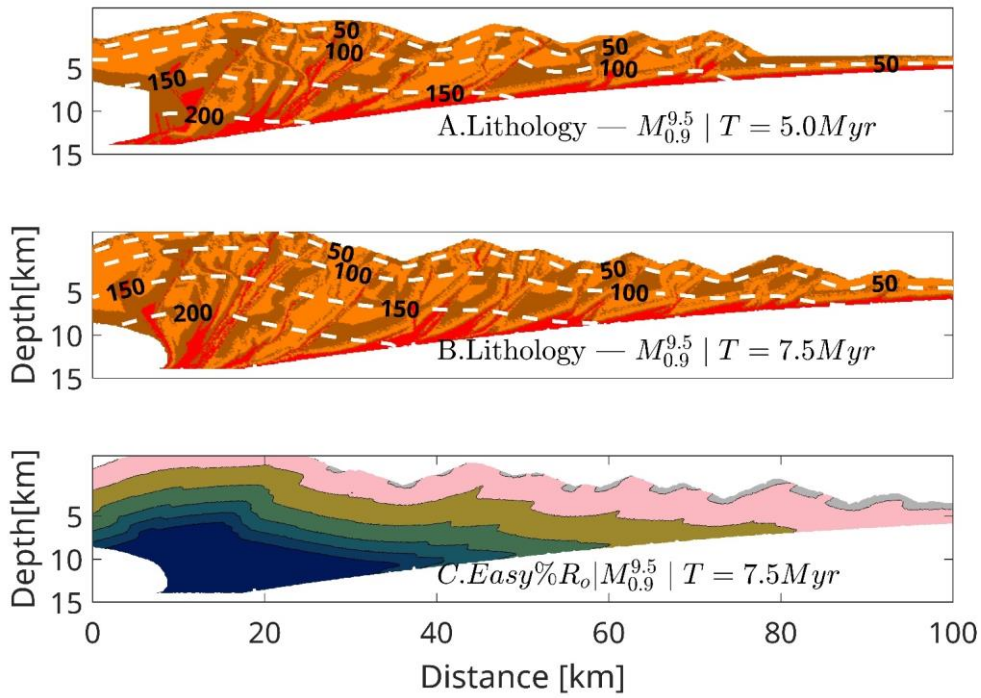


1120
 1121
 1122
 1123
 1124
 1125

1126

1127 **Fig. S13:**

1128 Typical thermomechanical evolution of the accretionary wedge for model $M_{0.9}^{9.5}$ at 5.0 Myr and 7.5 Myr of lithological evolution
1129 (Panel A-B). The dashed white lines represent the contours of the temperature field. The colormap for the first 2 panels is
1130 same as Figure 1. The Panel C represents thermal maturity values at ~ 7.5 Myr computed using Easy% R_o . The colormap for
1131 Panel E is same as that of Figure 3.
1132
1133



1134

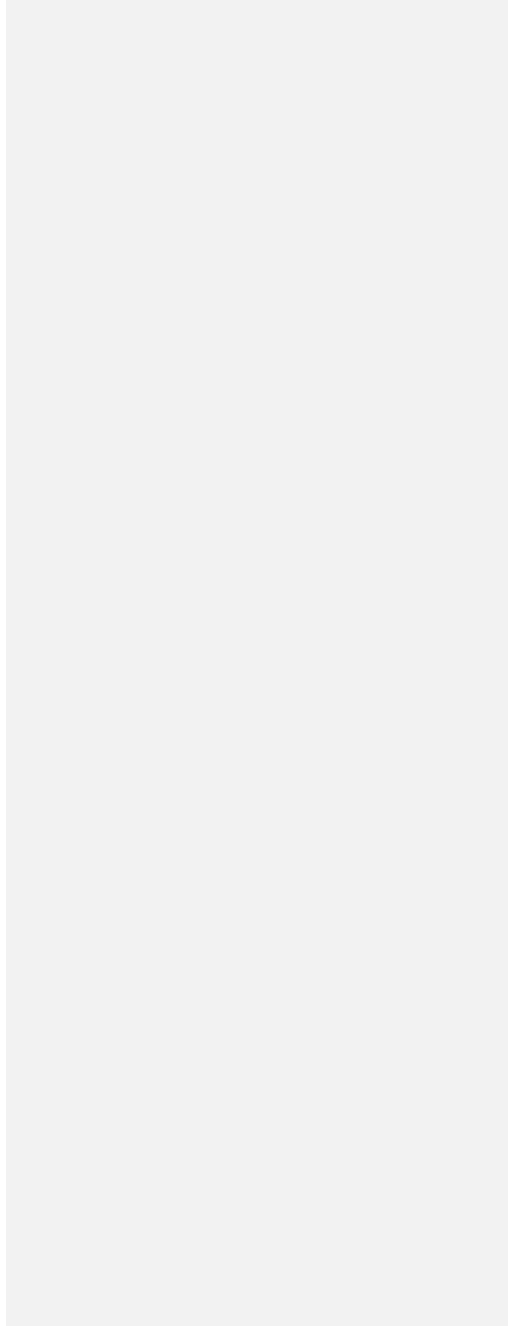
1135

1136

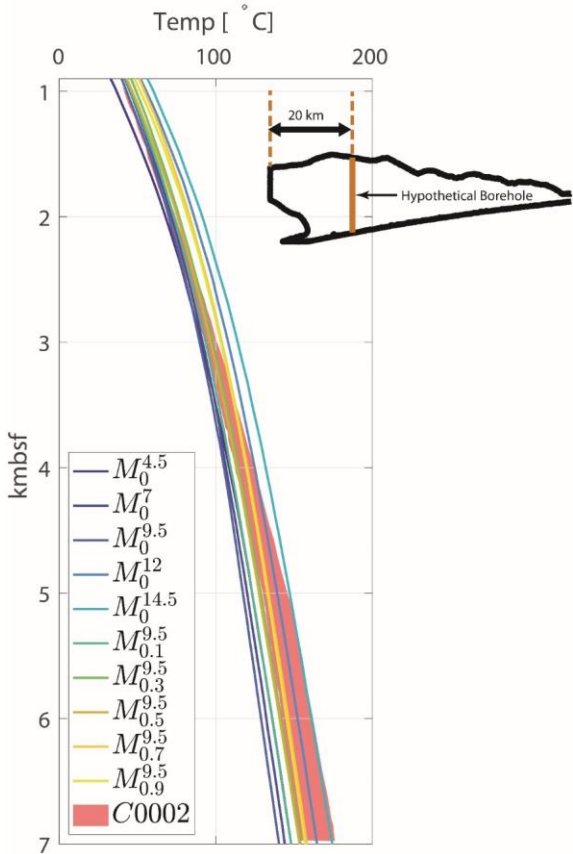
1137

1138

1139
1140
1141
1142
1143
1144
1145
1146
1147
1148
1149
1150
1151
1152
1153
1154
1155
1156
1157
1158



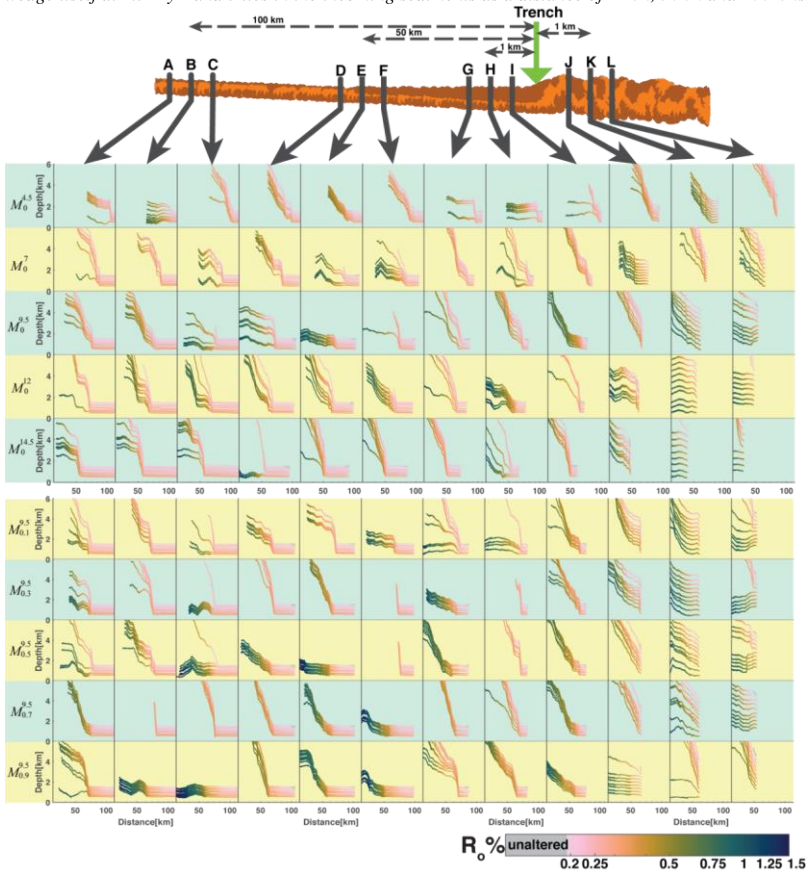
1159 **Fig. S14:**
 1160 *Plot of Temperature vs Depth profile in all models compared to Temperature-depth profile based on in-situ temperature from*
 1161 *the long-term borehole monitoring system (indicated red patch is the range of temperature estimated by (Sugihara et al.,*
 1162 *2014)). The temperature vs depth profiles for the models are computed for 20 kms from the backstop as shown in the inset.*
 1163
 1164



1165

1166 **Fig. S15**

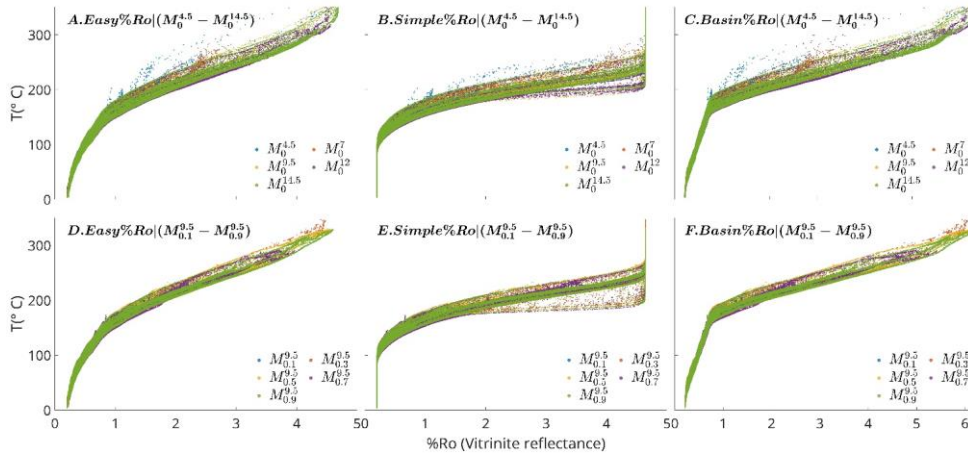
1167 *Trajectory of sediments in model. The wedge on top shows the location of individual boreholes relative to the position of the*
1168 *trench at 2.5 Myr. In each borehole, A-L 10 points are plotted for their trajectories between 2.5 Myr and 7.5 Myr. The color*
1169 *of markers in the trajectories represent the evolution of thermal maturity on individual sediment markers while undergoing*
1170 *evolution. The image of the wedge on top is a representative image showing the relative location of boreholes with respect to*
1171 *the trench and each other. We present 4 set of boreholes (each having 3 boreholes separated by a km), one of which lies in the*
1172 *wedge itself at 2.5 Myr and 3 lies in the incoming sediments as a distance of 1 km, 50km and 100 kms from trench.*



1173
1174

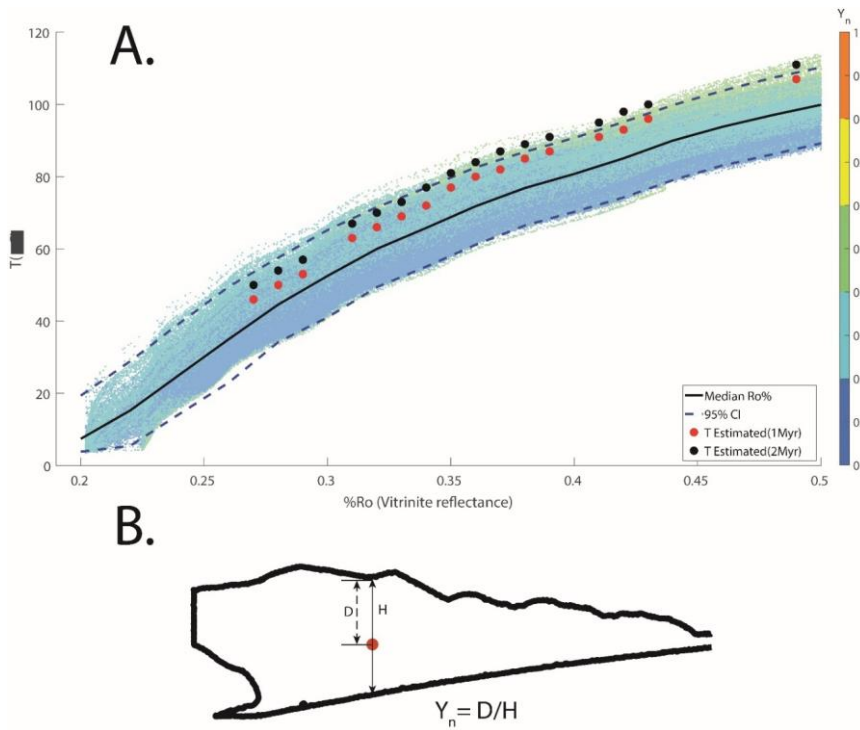
1175 **Fig. S16**

1176 *Vitrinite Reflectance(%R_v) vs Maximum Exposure temperature in models. Panel A, B and C show the Temperatures as a function of %R_v computed from Easy%R_v, Simple%R_v, Basin%R_v for models $M_0^{4.5} - M_0^{14.5}$. Similarly panels D, E and F show*
1177 *the Temperatures as a function of %R_v computed from Easy%R_v, Simple%R_v, Basin%R_v for models $M_{0.1}^{9.5} - M_{0.9}^{9.5}$.*
1178
1179
1180



1181
1182
1183
1184
1185
1186
1187
1188
1189
1190
1191
1192

1193 **Fig. S17:**
1194 Panel A shows %R_v vs T for model (shown by smaller markers) and C0002 borehole (shown by large circular markers)
1195 (Fukuchi et al., 2017). Y_n is the depth of the marker from the surface normalized by the thickness (vertical extent) of the wedge
1196 at the location of the marker as illustrated in Panel B.
1197

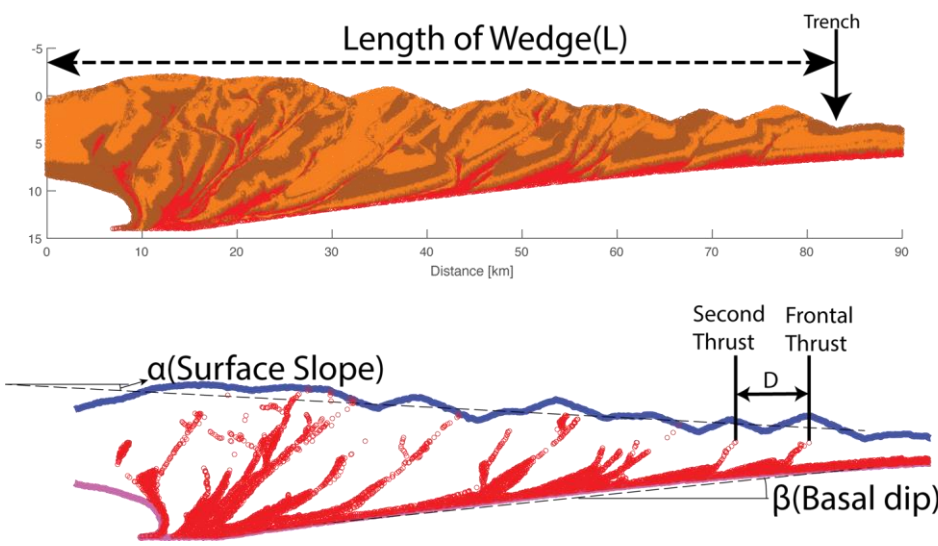


1198
1199
1200
1201
1202

1203 **Fig. S18:**

1204 Illustration to show the measurement of L (length of wedge), α (surface slope), β (basal dip) and D (Distance between the first

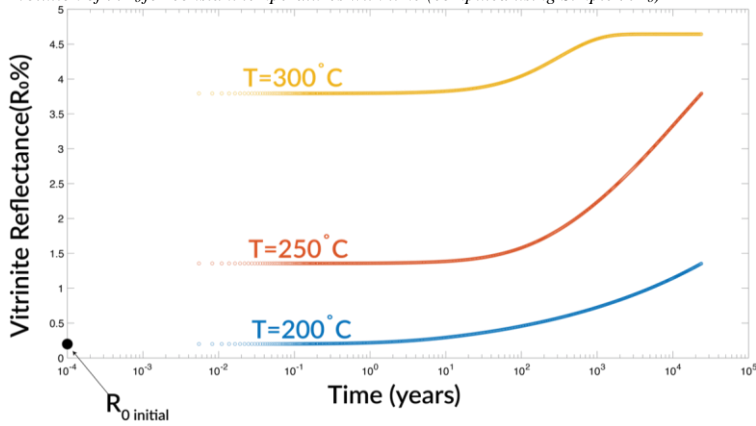
1205 and second frontal thrust).



1206
1207
1208
1209
1210
1211
1212
1213
1214
1215
1216
1217
1218

1219 **Fig S19:**

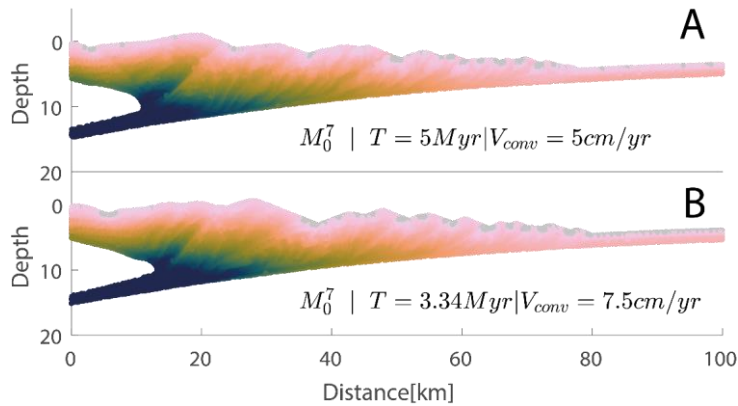
1220 Evolution of % R_o for constant temperatures with time (computed using Simple % R_o)



1221

1222 **Fig S20:**

1223 Thermal maturity distribution in two models with different convergent velocity. Panel A and B shows a models with convergent
1224 velocity of 5 cm/yr and 7.5 cm/yr respectively. The colormap for the images is same as for Figure 3. The comparison between
1225 the models has been shown for different time to keep the volume of incoming sediments ($T \cdot V_{conv}$) similar.



1226

1227

1228

229
230
231
232

Fig S21:

Distribution of viscosity in a representative model at 0.5 Myr, 2.5 Myr, 5.0 Myr and 7.5 Myr.

